Global Energy Interconnection xxx (2026) xxx–xxx

KeAi
CHINESE ROOTS
GLOBAL IMPACT

Global Energy Interconnection
Development and Cooperation Organization

Global Energy Interconnection

Contents lists available at ScienceDirect
journal homepage: www.elsevier.com/locate/gloei

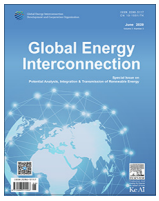

Momentum vectorized adaptive DDPG-based PSC mitigator design for hybrid PV-TEG systems with auxiliary battery participation

Lei Zhou [a], Bo Yang [a,*], Shuai Zhou [b], Hongbiao Li [c], Dengke Gao [c], Tek Tjing Lie [b], Lin Jiang [d]

[a] *Faculty of Electric Power Engineering, Kunming University of Science and Technology, Kunming 650500, China*
[b] *Department of Electrical and Electronic Engineering, Auckland University of Technology, Auckland 1010, New Zealand*
[c] *Shanghai KeLiang Information Technology Company Ltd., Shanghai 201103, China*
[d] *Department of Electrical and Electronic Engineering, University of Liverpool, Liverpool L69 3GJ, UK*

Received 20 September 2025; revised 18 December 2025; accepted 7 January 2026

Abstract

Partial shading conditions (PSC) significantly reduce the efficiency of photovoltaic (PV) systems by causing uneven irradiation and mismatched power losses. To address this, this study proposes a novel momentum vectorized adaptive deep deterministic policy gradient (MVA-ADDPG) algorithm for hybrid PV-thermoelectric generation (PV-TEG) systems. The PV-TEG system integrates thermoelectric generators with PV modules to capture waste heat and uses intelligent energy storage coordination to reduce temperature sensitivity and improve system stability. Unlike conventional PV-energy storage systems, which suffer from high energy losses and maintenance costs, the proposed MVA-ADDPG-driven PV-TEG system employs a triple-action heuristic exploration strategy. It combines momentum-accelerated policy gradients with dynamic exploration–exploitation balance. At each step, three candidate actions are evaluated, generated through both heuristic and gradient-based approaches., This enables fine-grained optimization of battery distribution and system performance. Experimental validation on 6 × 4 to 6 × 6 PV-TEG arrays show an average power increase of 26.5% and a mismatch loss reduction of 45.2%. The method achieves fast convergence and maintains reliable performance under varying shading conditions. By recovering waste heat and optimizing cell compensation, the proposed approach extends system lifespan, and enhances economic viability. It offers a robust solution for efficient energy management in complex PV environments.

Keywords: Hybrid PV-TEG systems; Multi-objective optimization; MVA-ADDPG; Reinforcement learning; SimuNPS; Thermoelectric power generation

0 Introduction

In recent years, the global energy crisis has intensified, and the imperative to address the ecological challenges posed by fossil fuels has become increasingly urgent. This has spurred a growing interest in the exploration and implementation of alternative energy sources. Among them, solar energy-being both clean and renewable has emerged as a pivotal focus in scientific and technological innovation [1,2].

Both technologies face critical challenges. Specifically, PV efficiency decreases under multi-peak curves induced by partial shading [3]. On the other hand, TEGs are limited by uneven temperature distributions—a phenomenon that significantly affects output voltage, internal resistance, and overall power stability [4]. TEGs recover PV waste heat to enhance energy utilization, and hybrid PV-TEG systems effectively mitigate respective limitations. Specifically, PV modules typically convert only 15–25% of solar

Peer review under the responsibility of Global Energy Interconnection Group Co. Ltd.
* Corresponding author.
E-mail addresses: 651060739@qq.com (L. Zhou), yangbo_ac@outlook.com (B. Yang).

https://doi.org/10.1016/j.gloei.2026.01.003

Nomenclature

Variables

V_{out}	output voltage
$V_{max,i}$	output voltage in the ith row
I_{out}	output current
T_{ref}	reference temperature
K	temperature compensation coefficient
$I_{comp,i}$	compensated current for the ith row
$I_{out,comp}$	total output current of PV array with battery participation
P_{PV}	maximum output power in PV array model
$\triangle T$	open circuit voltage
$S(T_{avg})$	Seebeck coefficient
T_{avg}	average temperature of TEG module
T_0	midpoint temperature between T_h and T_c
T_h	hot temperature of TEG module
T_c	cold temperature of TEG module
R_{in}	internal resistance
R_{load}	open-circuit voltage of column j
I_{TEG}	operating current
P_{out}	output power
$V_{total,j}$	open-circuit voltage of column j
$R_{total,j}$	total resistance value of column j
$R_{comp,j}$	internal resistance of battery
$V_{comp,j}$	additional voltage supplied by battery
$R_{eff,j}$	effective resistance
$V_{eff,j}$	effective voltage
I_{total}	total current
P_{out}	output power of hybrid PV-TEG systems
R_{total}	total resistance
P_{TEG}	maximum output power of TEG-battery system
V_{oc}	equivalent open-circuit voltage
T_p	surface temperature of PV module
T_e	ambient temperature
G	solar irradiance
v_f	ambient wind speed
$F_{PV\text{-}TEG}$	output power of the hybrid system
P_{Loss}	mismatch loss
P_{in}	relative improvement in system performance
G	solar irradiance
σ	reliability metric
Δx	reconfiguration increments
Q	Q-value of Q-Learning
r_t	reward or punishment of current action
s	current state
a	current action
γ	discount factor of current action
Δx	honey comb
$\mathscr{L}_{critic}$	centralized critic network

Abbreviations

A2C	advantage actor-critic
DQN	deep Q-network
HIL	hardware-in-the-loop
MVA-ADDPG	momentum vectorized adaptive deep deterministic policy gradient
MPPT	maximum power point tracking
PPO	proximal policy optimization
PSC	partial shading conditions
PSO	particle swarm optimization
PV	photovoltaic
SP	series–parallel
TCT	total cross-tied
TEG	thermoelectric generation

Parameters

M	number of rows in the model
N	number of columns in the model
$\mu\prime$	target networks
R	the impact of environmental factors

irradiance into electricity, with the majority dissipated as low-grade waste heat that TEGs can capture and convert into usable power, boosting the overall energy conversion efficiency of the system by 8–12% in practical deployments [3]. Moreover, the hybrid configuration complements PV's sensitivity to shading and TEG's low power density, delivering more stable and reliable output under dynamic environmental conditions, which is essential for meeting the demand for continuous power supply in distributed generation and off-grid applications.

Recent mitigation strategies for partial shading and thermal mismatch have progressed along divergent paths: PV research focuses on array reconfiguration [5] and adaptive maximum power point tracking (MPPT) [6] to mitigate mismatch losses, while TEG advancements prioritize automotive waste heat recovery [7] via advanced thermoelectric materials with enhanced ZT values [8,9]. For hybrid PV-TEG systems, current research primarily centres on three core aspects: optimization of system integration topology, refinement of coordinated control strategies, and performance validation under controlled laboratory conditions. However, practical implementations still face three critical barriers: 1) asynchronous optimization of electrical and thermal parameters, leading to inadequate synergy between PV power generation and TEG waste heat recovery [10]; 2) limited battery participation mechanisms that fail to adapt to dynamic irradiance and thermal gradients, resulting in suboptimal compensation effects [11]; 3) lack of full-scale validation of control strategies under real-world operating conditions, including

dynamic shading, variable ambient temperatures, and long-term operational degradation [12].

Analysis of key developments reveals persistent gaps: Yang et al. [3] implemented RL in PV-TEG systems but omitted dynamic compensation and HIL validation. Shao et al. [13] studied BIPV system performance under PSC but lacked TEG integration and dynamic compensation. Rasool et al. [14]'s improved MPPT algorithm showed 14.7% power variance under asymmetric shading. Studies [15–17] focused on PV array reconfiguration without battery-assisted coordinated control, while [18–20] adopted static current injection or predetermined voltage offsets, inadequate for $\Delta T > 15$ K thermal transients. Notably, while other researchers have indeed investigated partial shading mitigation in PV-TEG systems and attempted to develop improved algorithms (e.g., heuristic optimization for TEG array reconfiguration [6] or conventional RL for PV power regulation [11]) to enhance TEG performance, these efforts rarely address the coupled electrical-thermal dynamics of hybrid systems or integrate adaptive mechanisms for both shading and thermal mismatch. While prior studies have applied reinforcement learning to address partial shading in PV-TEG systems and explore TEG performance enhancement—such as adaptive twin-delayed DDPG for PV-TEG coordinated control [3], adaptive coordinated seekers for TEG dynamic reconfiguration under heterogeneous temperatures [21], and Q-Learning/PPO-based strategies for PV array mismatch mitigation [18,22]—none have specifically adopted MVA-ADDPG or analogous momentum-vectorized adaptive RL algorithms for thermoelectric modules.

Specifically, this study introduces a unified PV-TEG-battery configuration capable of simultaneously compensating current and voltage fluctuations. To manage this hybrid system under varying irradiance and thermal gradients, MVA-ADDPG algorithm is developed to balance fact convergence with robust exploration. This proposed framework is tested through a combination of array-level simulation and real-time HIL experiments. The findings of this study align well with practical PV-TEG operating scenarios, offering the thermoelectric community a solution to bridge simulation and real-world deployment. Quantitatively, the proposed battery-integrated system achieves an average 26.5% power increase and 45.2% mismatch loss reduction compared to PV-TEG systems without battery participationAs documented in literature [21], a practical dynamic reconfiguration case with embedded single-pole multiple-throw switches has been deployed in small-building PV systems, which aligns with our study's focus on mitigating the impact of partial shading via adaptive control.

The main contributions of this study are summarized as follows:

1) A reconfigurable PV-TEG-battery system featuring dynamic battery-based compensation was proposed. By coordinating parallel current injection at PV terminals and series voltage compensation across TEG arrays, this framework adapts in real time to row-specific thermal gradients.
2) A novel MVA-ADDPG algorithm is developed, integrating advantage-weighted policy gradient updates, tri-action constrained hybrid action spaces, and a dual-objective reward function. The controller effectively coordinates multi-agent interactions among PV, TEG and battery components to optimize overall power conversion and battery utilization.
3) A comprehensive validation setup, including simulation on $6 \times 4/6 \times 6$ arrays under 10 representative partial shading conditions, as well as HIL testing through RTLAB, is established to evaluate the proposed algorithm under diverse operational scenarios.

The remaining paper is structured as follows: Section 1 details the models of the hybrid PV-TEG system. Section 2 presents the compensation strategy using lithium iron phosphate battery. Section 3 designs a novel MVA-ADDPG controller for dynamic battery participation. Section 4 validates the designed algorithm through $6 \times 4/6 \times 6$ array simulations, Section 5 conducts HIL experiments for real-world evaluation. Finally, Section 6 concludes with key findings and future research directions.

1 System modelling

The hybrid PV-TEG system uses $M \times N$ Total Cross Tied (TCT) topology, shown in Figs. 1 and 2, where parallel rows enhance current output and series columns increase voltage. Compared to SP configurations, TCT reduces partial shading losses while maintaining uniform irradiation performance.

The output characteristics of the system at the maximum power point can be expressed as [20]:

$$V_{\text{out}} = \sum_{i=1}^{M} V_{\text{max},i} \tag{1}$$

$$I_{\text{out}} = \sum_{i=1}^{M} \sum_{j=1}^{N} (I_{i,j} - I_{i+1,j}) = 0 \tag{2}$$

where M and N represents the numbers of the rows and columns in the PV array, respectively; $I_{i,j}$ denotes the output current of the PV module at row i and column j, where the maximum output voltage is obtained.

The maximum output power of PV array model can be expressed as below [23]:

$$P_{\text{PV}} = \max\left(\sum_{j=1}^{N} \sum_{i=1}^{M} V_i I_i\right) \tag{3}$$

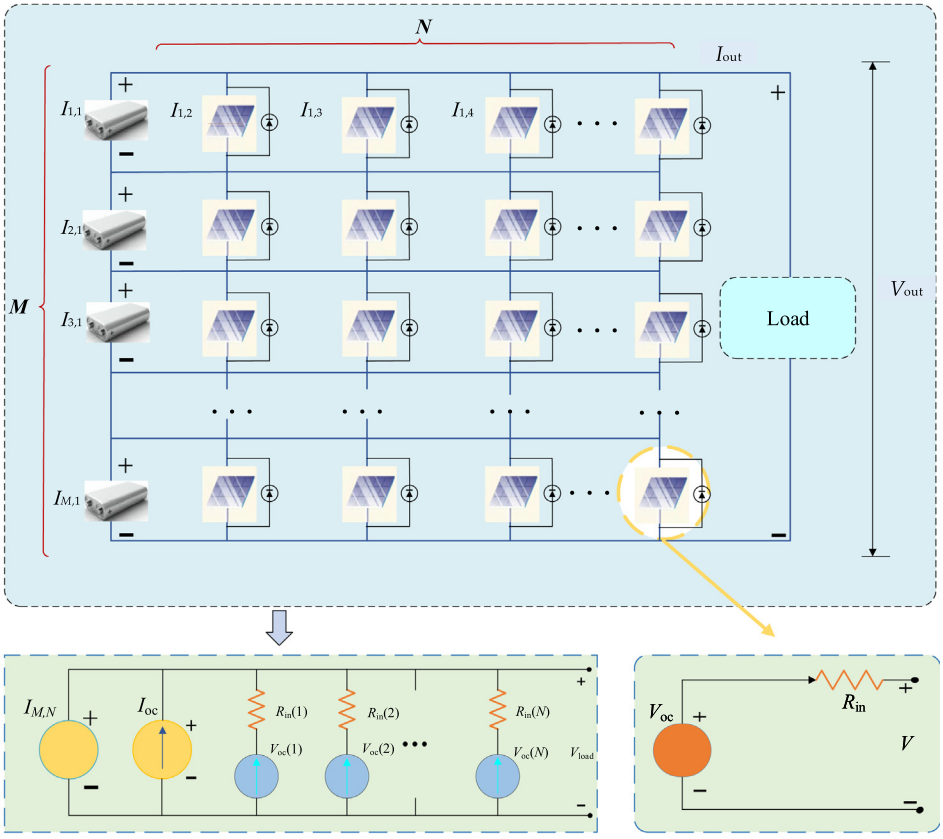

Fig. 1. Equivalent circuit and TCT connection structure of PV array.

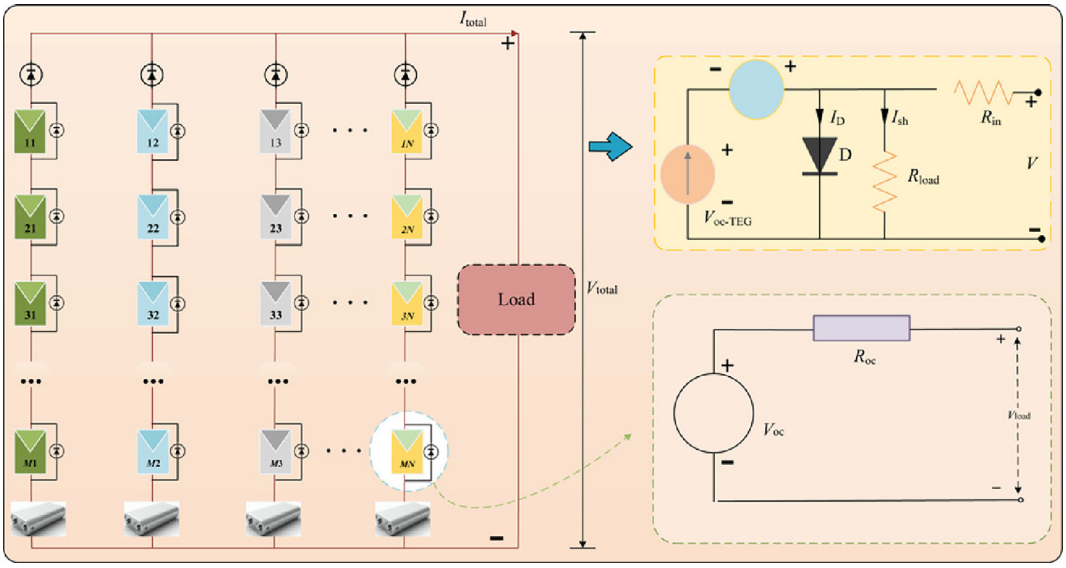

Fig. 2. $M \times N$ TEG connected array.

where V_i and I_i represent the voltage and current of the ith row, respectively.

Photovoltaic modules generate electricity while dissipating significant heat, which TEGs harness through the Seebeck effect by converting PV waste heat into electrical energy via temperature gradients (ΔT). As shown in Fig. 2, TEGs employ the same TCT topology for enhanced thermal-electrical coupling.

The hybrid PV-TEG system adopts a commercial monocrystalline silicon PV module (A10 Green Technology AJ-M60-225) with each PV cell sized 156.75 mm × 156.75 mm (assembled into a 1650 mm × 992 mm module), and a TEG module (TGM199-1.4-2.0) with an overall dimension of 40 mm × 40 mm × 4.4 mm, including TE legs with a height of 1.4 mm and width of 1.0 mm, 199 pairs of TE legs, ceramic substrates with a thickness of 0.15 mm (each side), and copper electrodes with a thickness of 0.25 mm (each side).

The open circuit voltage generated by a TEG, denoted as $V_{\mathrm{oc-TEG}}$ can be expressed as:

$$V_{\mathrm{oc-TEG}} = \Delta T \cdot S(T_{\mathrm{avg}}) \tag{4}$$

where ΔT represents the temperature difference between the hot side T_{h} and cold side T_{c} and $S(T_{\mathrm{avg}})$ denotes the Seebeck coefficient, which depends on the average temperature T_{avg} of TEG. In this study, the Seebeck coefficient is given by:

$$S(T_{\mathrm{avg}}) = S_1 + S_2 \ln \frac{T_{\mathrm{avg}} - T_0}{T_{\mathrm{h}} - T_{\mathrm{c}}} \tag{5}$$

where$S_1 = 210$ μV/K and$S_2 = 120$ μV/K; T_0 is the midpoint temperature between T_{h} and T_{c}. This formulation captures the non-linear behavior of the Seebeck coefficient under variable thermal conditions. This could enable more accurate estimation of TEG's electrical output. Specifically, the TEG modules adopt bismuth telluride (Bi_2Te_3)-based thermoelectric materials, with a thermal conductivity of 1.2 W/(m·K), an electrical conductivity of 1.0×10^5 S/m, and a ZT value of 0.8 at 200 °C, whereas the PV modules are fabricated from monocrystalline silicon with an electrical conductivity of 2.3×10^4 S/m and a thermal conductivity of 148 W/(m·K).

In this study, the internal resistance R_{in} is also considered in TEG and is expressed as a function of the average temperature:

$$R_{\mathrm{in}}(T_{\mathrm{avg}}) = R_1 + R_2 \cdot T_{\mathrm{avg}} \tag{6}$$

where $R_1 = -2.579\ \Omega$ and $R_2 = 0.014\ \Omega$/K, reflecting the impact of environmental factors on the electrical performance [24].

The operating current I_{TEG} through TEG, when connected to an external load R_{load} is:

$$I_{\mathrm{TEG}} = \frac{V_{\mathrm{oc}}}{R_{\mathrm{load}} + R_{\mathrm{in}}(T_{\mathrm{avg}})} \tag{7}$$

To maximize the output power, the load resistance should match the internal resistance. The output power delivered to the load is then:

$$P_{\mathrm{out-TEG}} = I_{\mathrm{TEG}}^2 \cdot R_{\mathrm{load}} \tag{8}$$

For a system with multiple TEG modules arranged in columns, the total current I_{total} and effective resistance R_{total} are [25]:

$$I_{\mathrm{total}} = \sum_{j=1}^{N} \frac{V_{\mathrm{total},j}}{R_{\mathrm{total},j}}, R_{\mathrm{total}} = \left(\sum_{j=1}^{N} \frac{1}{R_{\mathrm{in}}(j)} \right)^{-1} \tag{9}$$

Finally, the equivalent open-circuit voltage V_{oc} and maximum output power P_{TEG} of TEG subsystem are defined by [25,26]:

$$V_{\mathrm{oc}} = I_{\mathrm{total}} \cdot R_{\mathrm{total}} \tag{10}$$

$$P_{\mathrm{TEG}} = \frac{(0.5 I_{\mathrm{total}} \cdot R_{\mathrm{total}})^2}{R_{\mathrm{total}}} \tag{11}$$

Accurate modeling of PV-TEG systems requires considering PV surface temperature T_{p}, which critically impacts efficiency [27]. PV efficiency decreases exponentially with T_{p}, while TEG temperature difference (ΔT) increases linearly, creating a coupled thermal-electrical relationship. This critical coupling parameter can be expressed as follows:

$$T_{\mathrm{p}} = 0.943 T_{\mathrm{e}} + 0.0195 G - 0.528 v_{\mathrm{f}} + 0.3529 \tag{12}$$

where T_{e} is the ambient temperature, which has a strong influence on T_{p}; G represents solar irradiance, contributing to temperature rise through energy absorption, and v_{f} denotes the ambient wind speed, which provides a cooling effect by enhancing convective heat loss. The constant terms account for additional thermal and design-related factors of PV module [28,29].

The output power of hybrid PV-TEG system is expressed as:

$$P_{\mathrm{out}} = P_{\mathrm{PV}} + P_{\mathrm{TEG}} \tag{13}$$

where P_{PV} and P_{TEG} are the total output power contributions from PV and TEG subsystems, respectively.

2 Modelling of hybrid PV-TEG system with battery participation

The proposed hybrid PV-TEG system introduces a bidirectional battery participation mechanism to address power mismatch and parameter configuration challenges. As shown in Fig. 3, this innovation employs lithium iron phosphate batteries for dual-path regulation: acting as parallel current sources in PV arrays to mitigate temperature-induced current deviations, while functioning as series voltage sources in TEG columns to suppress thermal gradient voltage fluctuations. The left panel illustrates the $LiFePO_4$ battery's internal structure, while the right depicts the integrated framework with batteries integrated row-wise in PV and TEGs arranged column-wise at cold terminals. This coordinated approach overcomes traditional single-compensation limitations, enabling simultaneous electrical-thermal optimization through dynamic bidirectional control.

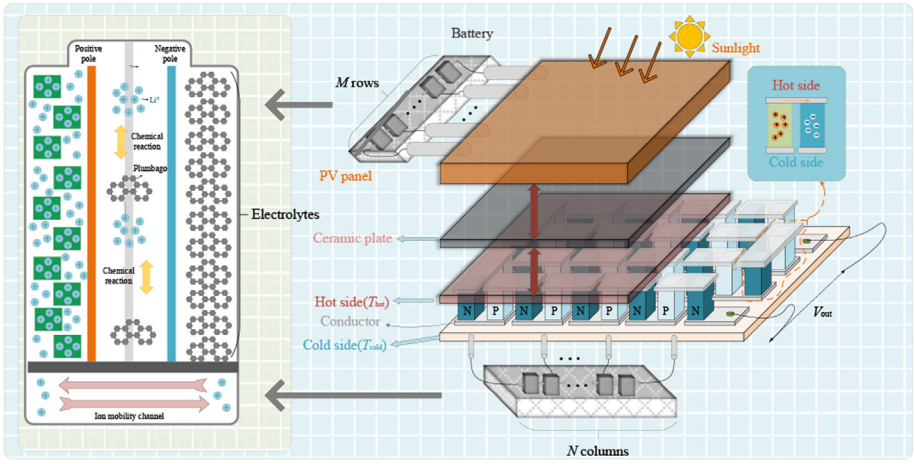

Fig. 3. The proposed hybrid PV-TEG system with auxiliary battery participation.

Initially, P_{max} is defined as the maximum output power with battery participation. The total compensated power P_{comp} of all cells is then calculated based on the optimal compensation action of each cell, P_{pure} shows that the value of net output power excluding compensation.

$$P_{max} = P_{pure} + P_{comp} \tag{14}$$

The compensated current $I_{comp,i}$ for the ith row can be expressed as:

$$I_{comp,i} = K \cdot (T_{ref} - T_i) \tag{15}$$

where K is the temperature compensation coefficient, T_{ref} is the reference temperature, and T_i is the temperature of the ith row. The total output current of PV array with battery participation is then given by:

$$I_{out,comp}(t) = I_{out}(t) + \sum_{i=1}^{M} I_{comp,i}(t) \cdot f(\mathrm{SoC}(t)) \tag{16}$$

The results demonstrate that the battery participation mechanism enhances the stability and reliability of PV system under various conditions, whilst concomitantly improving the efficiency of TCT topology. The TEG model incorporates battery participation to address temperature-dependent Seebeck coefficient variations and internal resistance, thereby optimizing power generation through the conversion of thermal energy into electrical energy and the stabilization of voltage output [30,31].

To accurately describe the dynamic characteristics and long-term operational impacts of lithium-ion batteries, the State of Charge (SoC) constraints and degradation factor model are integrated into the system. SoC is defined as the ratio of the battery's remaining capacity to its rated capacity, serving as a core indicator for safe and efficient operation. Its dynamic evolution is governed by charging/discharging behavior, self-discharge, and efficiency variations:

$$\mathrm{SoC}(t) = \mathrm{SoC}_0 + \frac{1}{C_n}\int_0^t \left(\eta_c I_c(\tau) - \frac{I_d(\tau)}{\eta_d} - I_{self}(\tau)\right) d_\tau \tag{17}$$

where SoC_0 is the initial SoC (set to 0.5 for initialization), C_n denotes the battery's rated capacity, η_c (0.95) and η_d (0.92) are the charging and discharging efficiencies, and $I_c(\tau)$, $I_d(\tau)$, and $I_{self}(\tau)$ (0.02 A) are the charging current, discharging current, and self-discharge current, respectively. To avoid overcharging/over-discharging induced degradation, SoC is constrained within a safe range: $0.1 \le \mathrm{SoC}(t) \le 0.9$.

Additionally, the charging/discharging currents are limited by the battery's rated parameters (Table 1): $|I_c|$<10 A and $|I_d|$ A. When $\mathrm{SoC}(t)$ approaches the boundary values, the compensation current/voltage is linearly scaled down via a correction factor $f(\mathrm{SoC}(t))$:

$$f(\mathrm{SoC}(t)) = \begin{cases} 0 & \mathrm{SoC}(t) < 0.2 \text{or} \, \mathrm{SoC}(t) > 0.8 \\ \frac{\mathrm{SoC}(t)-0.2}{0.6} & 0.2 \le \mathrm{SoC}(t) \le 0.5 \\ \frac{0.8-\mathrm{SoC}(t)}{0.6} & 0.5 < \mathrm{SoC}(t) \le 0.8 \end{cases} \tag{18}$$

In our enhanced model, each column of TEG array is treated as a series of interconnected current sources, The rows and columns are indexed by i and j, respectively. The total voltage $V_{total,j}$ and total resistance $R_{total,j}$ in the j th column are calculated by summing the individual values across all rows, as shown in the following equation:

$$V_{total,j} = \sum_{i=1}^{N} V_{i,j}, R_{total,j} = \sum_{i=1}^{N} R_{i,j} \tag{19}$$

To further enhance the output power, a battery is integrated at the bottom of each column. The battery provides an additional voltage $V_{comp,j}$ and has an internal resistance $R_{comp,j}$. The effective voltage $V_{comp,j}$ and effective resistance $R_{eff,j}$ for column j are then given by

$$V_{eff,j} = V_{total,j} + V_{comp,j} \tag{20}$$

$$R_{eff,j} = R_{total,j} + R_{comp,j} \tag{21}$$

Table 1
Model parameters setting.

Parameter	Value or Types
PV product model	A10 Green Technology AJ-M60-225
Battery type	$LiFePO_4$battery
Part of TEG product model	TGM199-1.4-2.0
PV maximum power per module/W	224.9856
TEG maximum output per power/W	7.3
PV open circuit voltage per module/V	36.24
TEG open circuit voltage per module/V	11
PV open circuit current per module/A	8.04
TEG open circuit current per module/A	2.65
Voltage at the maximum power point per module/V	30.24
Current at the maximum power point per module/A	7.44
TEG parameter measurement condition/℃	$T_c = 30$, $T_h = 200$
Size of module/mm	40 × 40 × 40
Nominal battery voltage/V	32
Maximum battery charging current/A	30
Maximum battery discharge current/A	20

The $LiFePO_4$ battery (Fig. 3) is selected for its superior thermal stability, extended cycle life, and flat discharge curve (Eq. (20)). The combination of these properties enables precise voltage regulation with minimal resistive losses. Its wide operating temperature range corresponds with PV-TEG thermal gradients, while the battery's low self-discharge rate and its cobalt-free composition enhance sustainability. These attributes optimize compensation efficacy by mitigating temperature-induced fluctuations (Eq. (16)), ensuring resilient energy harvesting under dynamic environmental conditions.

As the role of battery participation in enhancing system stability has not been addressed in existing literature [9], this forms the focus of the present discussion. Lyapunov stability analysis is extended to incorporate SoC constraints and degradation factors. The modified Lyapunov function considers both compensation current and SoC deviations:

$$V = \frac{1}{2}\sum_{i=1}^{M} I_{\mathrm{comp},i}^2 + \frac{1}{2}(\mathrm{SoC}(t) - 0.5)^2 \tag{22}$$

The next step is to calculate the derivative of V:

$$\frac{\mathrm{d}V}{\mathrm{d}t} = \sum_{i=1}^{M} I_{\mathrm{comp},i}\left(-K\frac{\mathrm{d}T_i}{\mathrm{d}t}\right) + (\mathrm{SoC}(t) - 0.5)\cdot\frac{\mathrm{dSoC}(t)}{\mathrm{d}t} \tag{23}$$

If the temperature change $\frac{\mathrm{d}V}{\mathrm{d}t}$ and the compensation current $I_{\mathrm{comp},i}$ have the same sign (i.e., the compensation current decreases when temperature rises and increases when temperature falls), then $\frac{\mathrm{d}V}{\mathrm{d}t} < 0$, satisfying the Lyapunov stability condition. Therefore, the system is asymptotically stable.

The battery participation mechanism has been demonstrated to enhance the efficiency and reliability of the system. In order to quantify the enhancement of system reliability by battery participation, a reliability metric σ is introduced:

$$\sigma = 1 - \frac{\sum_{i=1}^{M}|I_{\mathrm{out},i} - I_{\mathrm{comp},i}|}{M\cdot I_{\mathrm{out},i}}\cdot\frac{\sum_{j=1}^{N}|V_{\mathrm{total},j} - V_{\mathrm{comp},j}|}{N\cdot V_{\mathrm{total},j}} \tag{24}$$

In the case of σ approximating one, it can be deduced that the system's output current is characterized by a notable level of stability and reliability. Conversely, when σ approaches zero, it is indicative of significant fluctuations in the output current, which in turn can compromise the reliability of the system. The negative qualitative proof of the derivative of the Lyapunov function allows a rigorous demonstration that the system is in a steady state for a given range of temperature fluctuations.

Battery degradation is dominated by two mechanisms: cycle aging and calendar aging. The total capacity degradation rate α_{deg} is quantified as:

$$\alpha_{\mathrm{deg}}(t) = \alpha_{\mathrm{cycle}}\cdot N_{\mathrm{eq}}(t) + \alpha_{\mathrm{cal}}\cdot t \tag{25}$$

where $\alpha_{\mathrm{cycle}} = 2.5\times10^{-4}$ per cycle (cycle degradation coefficient), $N_{\mathrm{eq}}(t)$ is the equivalent number of cycles, $\alpha_{\mathrm{cal}} = 1.2\times10^{-6}$ per hour (calendar degradation coefficient), and t is the cumulative operational time (h).

The actual available capacity of the battery after degradation is:

$$C(t) = C_n\cdot(1 - \alpha_{\mathrm{deg}}(t)) \tag{26}$$

where a minimum available capacity threshold of C_n is set to ensure system performance; when $C(t) < 0.8C_n$, the battery is deemed to have reached the end of its service life.

3 Design of MVA-ADDPG

To address the optimization needs of PV-TEG systems, MVA-ADDPG algorithm is proposed in this section to coordinate the regulation of current and voltage compen-

sation. The motivation for improving the algorithm stems from resolving asynchronous electrical-thermal optimization and insufficient dynamic compensation under PSC, where momentum vectorized policy gradient stabilizes training convergence and tri-action exploration enhances compensation precision—both jointly promoting PV-TEG-battery coordination, while hyperparameter-level enhancements such as adaptive learning rate scheduling could be further investigated.

The algorithm parameters were determined via iterative tuning across 10 typical shading scenarios and ablation experiments to balance performance metrics, and altering these values (e.g., increasing β beyond 0.9 or reducing α below 0.1) would degrade convergence speed or optimization upper limit, while slight adjustments within ±20% of the optimal values show no significant performance improvement.

The objective function is proposed to optimize the dynamic reconfiguration of hybrid PV-TEG Systems. This algorithm integrates multi-agent coordination with adaptive value estimation to maximize the output power, while satisfying row-column switching constraints and irradiance consistency (Eq. (23)) [32].

To explicitly define MVA-ADDPG algorithm, two core mechanisms are formalized as follows:

1) Momentum vectorized policy gradient: the momentum term is embedded into the policy update rule to stabilize gradient descent, expressed as

$$\nabla_\theta J(\theta) = \beta \cdot \nabla_\theta J(\theta_{t-1}) + (1-\beta) \cdot \nabla_\theta \log \pi_\theta(a_t|s_t) Q(s_t, a_t) \tag{27}$$

where $\beta = 0.9$ denotes the momentum coefficient, θ is the policy network parameter, $\pi_\theta(a_t|s_t)$ is the policy distribution, and $Q(s_t, a_t)$ is the action-value function.

2) Tri-action heuristic exploration strategy: at each iteration, three candidate actions are generated and evaluated:

$$a_{\text{heur},t} = [K \cdot (T_{\text{ref}} - T_i), K' \cdot \Delta T_j] \tag{28}$$

$$a_{\text{grad},t} = \mu_\theta(s_t) + \mathcal{N}(0, \sigma_t^2) \tag{29}$$

$$a_{\text{hyb},t} = \alpha_t \cdot a_{\text{heur},t} + (1-\alpha_t) \cdot a_{\text{grad},t} \tag{30}$$

where K is empirical current compensation coefficient for PV rows, linking compensation to the temperature deviation between the reference temperature T_{ref} and the actual temperature T_i of the i-th PV row; K' is empirical voltage compensation coefficient for TEG columns, associating compensation with the temperature difference ΔT_j of the j-th TEG column; α_t shows weight coefficient that linearly decreases from 0.7 to 0.1 during training--prioritizes heuristic guidance in early exploration, and gradient-based optimization in late exploitation (Fig. 4).

The calculation of the mismatch loss P_{Loss} can be expressed as follows:

$$P_{\text{Loss}} = P_0 - P_{\max} \tag{31}$$

$$F_{\text{PV-TEG}} = \max(P_{\text{PV}} + P_{\text{TEG}} - P_{\text{Loss}}) \tag{32}$$

The switching mechanism adheres to strict permutation constraints across photovoltaic columns and thermoelectric rows, employing discrete adjustment vectors guided by solar irradiance patterns to reconfigure system topology while minimizing power losses through coordinated spatial adaptation, it could be expressed [33,34]:

$$\bigcup_{i=1}^{M} x_{\text{PV}}(i,j) = \{1, \ldots, M\} \tag{33}$$

$$\bigcup_{j=1}^{N} x_{\text{TEG}}(i,j) = \{1, \ldots, N\} \tag{34}$$

$$a_t = [\Delta x_{\text{PV}}(i,j), \Delta x_{\text{TEG}}(i,j)], \Delta x \in \{-1, 0, 1\} \tag{35}$$

where Δx_{PV} and Δx_{PV} denote column-wise of PV and row-wise of TEGs reconfiguration increments; $I_{\text{irradiance}}(i,j)$ represents the irradiance distribution [35].

The reward combines power maximization and irradiance consistency:

$$\begin{aligned} r_t = (P_{\text{PV}} + P_{\text{TEG}} - P_{\text{Loss}}) - \lambda_1 \|Q(s,a) - Q'(s,a)\|^2 \\ -\lambda_2 \cdot \alpha_{\text{deg}}(t) - \lambda_3 \cdot |\text{SoC}(t) - 0.5| \end{aligned} \tag{36}$$

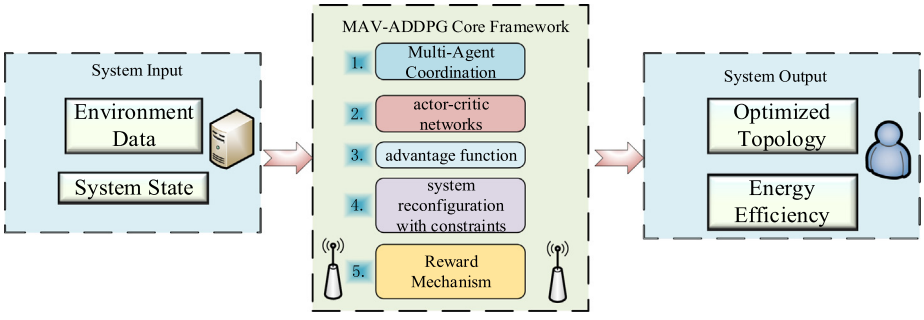

Fig. 4. MVA-ADDPG schematic diagram.

where λ_2 and λ_3 are penalty weights (recommended range: 0.1 $\sim$ 0.3), guiding the algorithm to prioritize compensation strategies with SoC within the middle range and minimal degradation.

The centralized critic network is updated via TD error:

$$\mathscr{L}_{\text{critic}} = \mathbb{E}\left[\left(Q(s_t, a_t) - \left(r_t + \gamma Q'(s_{t+1}, \mu'(s_{t+1}))\right)\right)^2\right] \tag{37}$$

where γ is the discount factor controlling the decay rate of future rewards; μ' and Q' both are target networks.

Other algorithms addressing PSC in PV-TEG systems include DQN (good for discrete actions but poor for continuous compensation), PPO (stable but inefficient in exploration), and A2C (weak stability), while MVA-ADDPG balances fast convergence, high compensation precision, and adaptability to dynamic thermal-electrical gradients.

The framework of MVA-ADDPG employs multi-agent reinforcement learning to dynamically compensate PV-TEG rows or columns, mitigating partial shading and thermal mismatch losses while optimizing energy harvesting efficiency, as illustrated in Fig. 5.

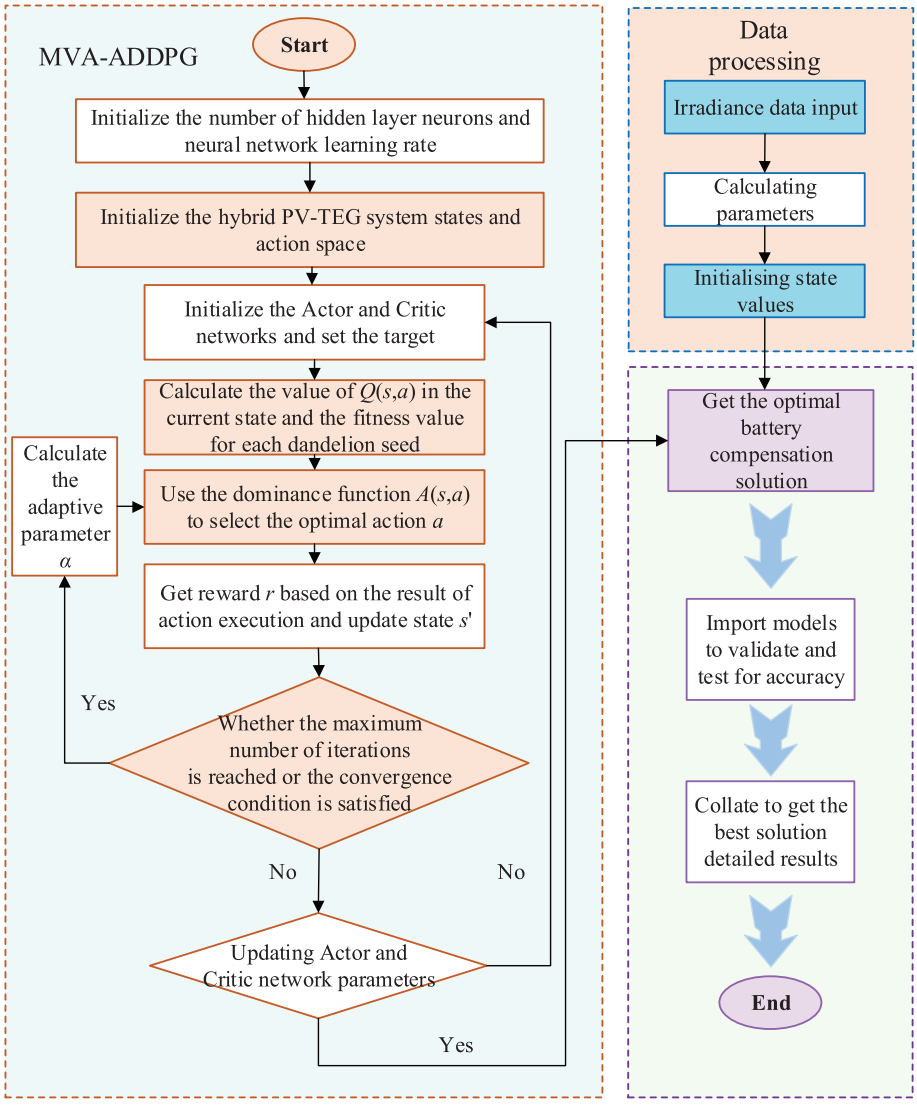

Fig. 5. MVA-ADDPG flowchart.

Table 2
Algorithm parameter setting.

Name of algorithms	Parameters	Symbol	Value
MVA-ADDPG [37]	Inertia weight	ω	0.5
	Self-awareness learning factor	C_1	1.5
	Social learning factor	C_2	1.5
	Learning rate	α	0.1
DQN [38]	Exploration rate	E_λ	0.1
	Attraction coefficient base value	β	1.2
PPO [39]	Delta	Δ	0.7
	Gamma	γ	0.9
A2C [40]	Actor learning rate	α_{actor}	0.01
	Critic learning rate	α_{critic}	0.1

4 Simulation results

This study evaluates MVA-ADDPG for optimizing PV-TEG Systems under partial shading. Experiments were conducted on two configurations: a 6 × 4 array and a 6 × 6 array, representing different energy harvesting scenarios. The proposed method was rigorously compared with three RL algorithms: DQN, PPO, and A2C, under uniform hyperparameters ($N = 50, \text{Iter} = 200$). Simulations under controlled conditions (TEG cold-end: 25 °C, wind speed: 1.5 m/s laminar flow) analysed PV-TEG material properties (Table 1) and reinforcement learning parameters (Table 2) per [36], with MATLAB/Simulink 2023b and SimNPS models executed on a standard PC (Intel® i5, 16 GB RAM) using variable-step ode45 solver.

4.1 Scenario I: 6 × 4 asymmetrical array under PSC

MVA-ADDPG algorithm demonstrates superior computational performance in optimizing a 6 × 4 asymmetric PV-TEG systems under ten shading patterns (uneven row, uneven column, short-width, etc.), achieving 34.70% and 46.62% power optimization efficiencies in short-width and short-narrow configurations (Tables A3 and A4), outperforming DQN, PPO and A2C by 3–5 percentage points in η-values. Notably, it maintains >15% efficiency in complex scenarios (e.g., diagonal layouts), while alternatives like PPO degrade to 5.52% in long-width cases, highlighting its stability in heterogeneous power allocation. The compensation mechanisms between PV-TEG ranks (Tables A1 and A2) and electrical characteristics under ten conditions are systematically analysed, and 10 typical irradiance distributions in Fig. B1 correspond to *P-V* and *I-V* curves of PV (Fig. 6) and TEG (Fig. 7) subsystems after battery voltage-current compensation. As demonstrated in Figs. 8 and 9, the mismatch loss summary and

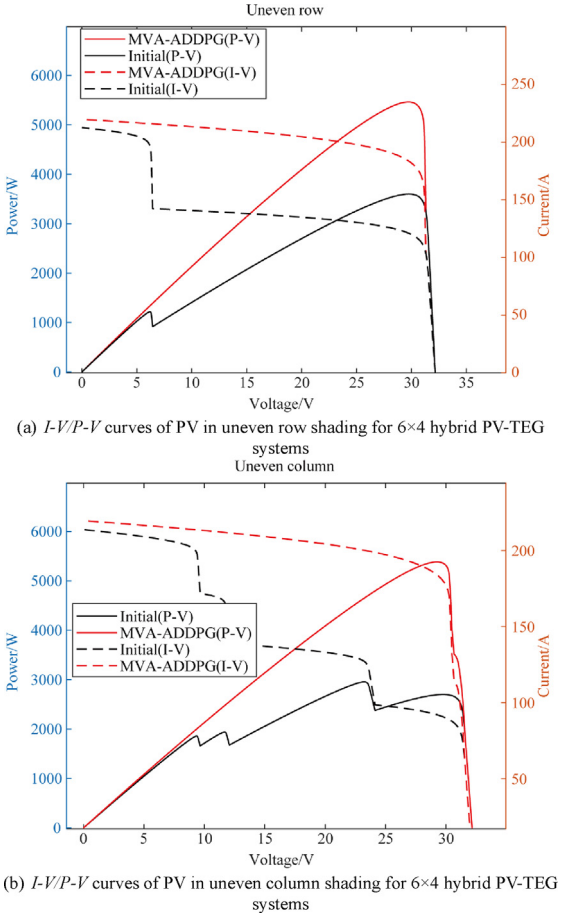

(a) *I-V/P-V* curves of PV in uneven row shading for 6×4 hybrid PV-TEG systems

(b) *I-V/P-V* curves of PV in uneven column shading for 6×4 hybrid PV-TEG systems

Fig. 6. *I-V* and *P-V* plots of the part of PV in 6 × 4 hybrid PV-TEG systems at ten irradiances under standard PSC.

iterative plots provide a clear representation of 6 × 4 hybrid PV-TEG systems.

As shown in Fig. 9(a), the newly added PSO algorithm iteration curve (parameter settings: inertia weight$\omega = 0.7$,

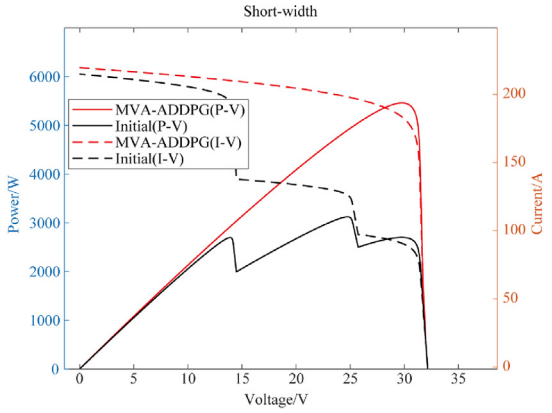

(c) *I-V/P-V* curves of PV in short-width shading for 6×4 hybrid PV-TEG systems

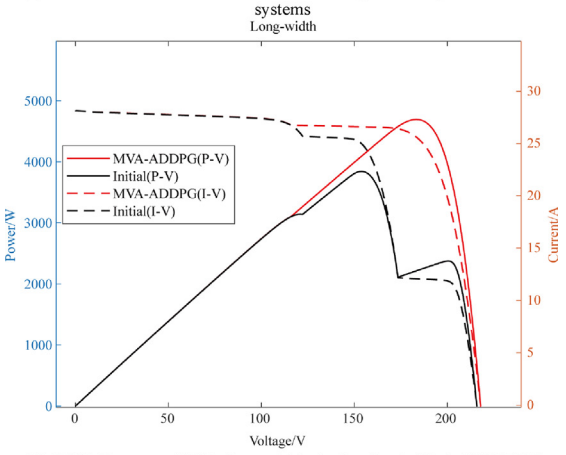

(d) *I-V/P-V* curves of PV in long-width shading for 6×4 hybrid PV-TEG systems

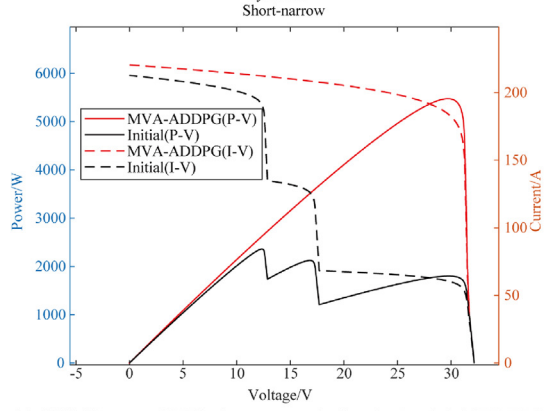

(e) *I-V/P-V* curves of PV in short-narrow shading for 6×4 hybrid PV-TEG systems

Fig 6. *(continued)*

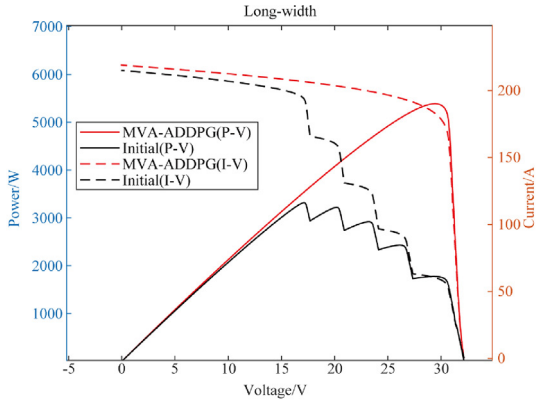

(f) *I-V/P-V* curves of PV in long-narrow shading for 6×4 hybrid PV-TEG systems

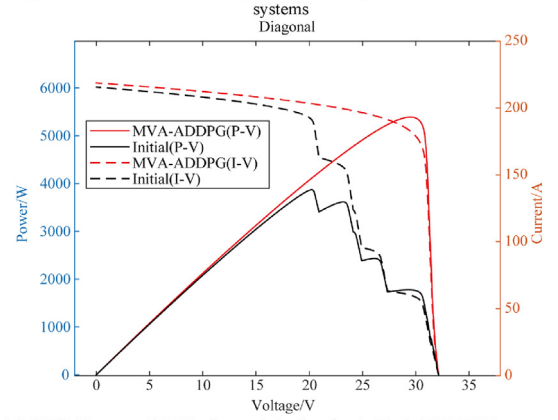

(g) *I-V/P-V* curves of PV in diagonal shading for 6×4 hybrid PV-TEG systems

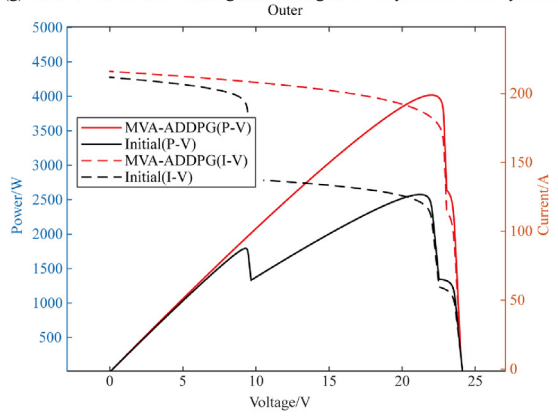

(h) *I-V/P-V* curves of PV in outer shading for 6×4 hybrid PV-TEG systems

Fig 6. *(continued)*

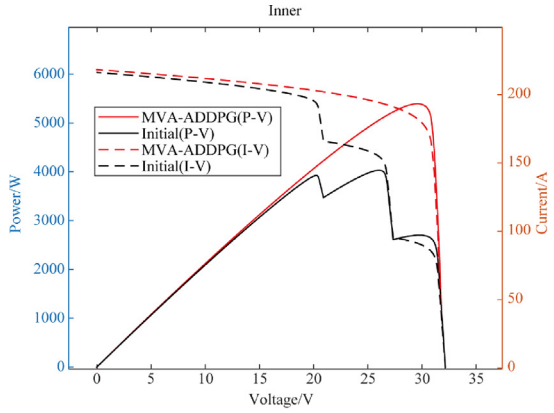

(i) *I-V/P-V* curves of PV in inner shading for 6×4 hybrid PV-TEG systems

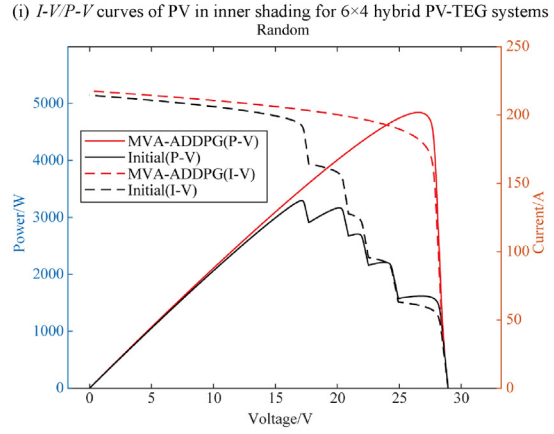

(j) *I-V/P-V* curves of PV in random shading for 6×4 hybrid PV-TEG systems

Fig 6. *(continued)*

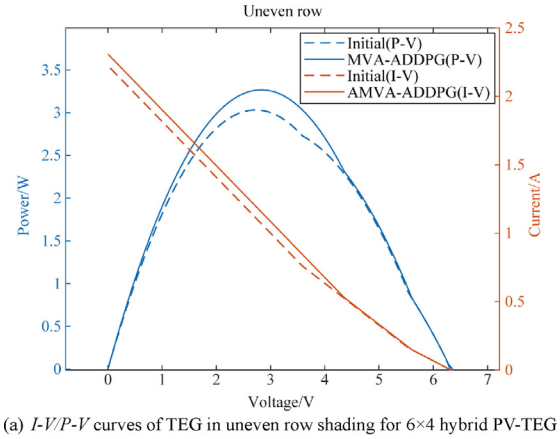

(a) *I-V/P-V* curves of TEG in uneven row shading for 6×4 hybrid PV-TEG systems

Fig. 7. *I-V* and *P-V* plots of the part of TEG in 6 × 4 hybrid PV-TEG systems at ten irradiances under standard PSC.

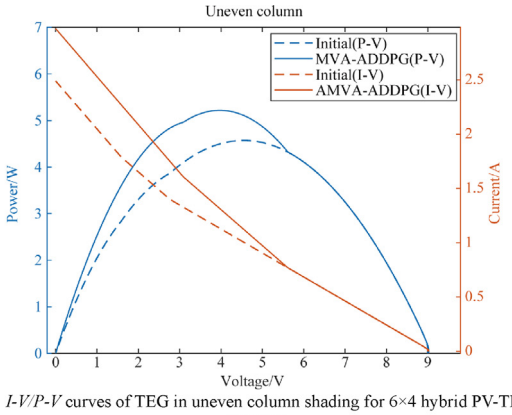

(b) *I-V/P-V* curves of TEG in uneven column shading for 6×4 hybrid PV-TEG systems

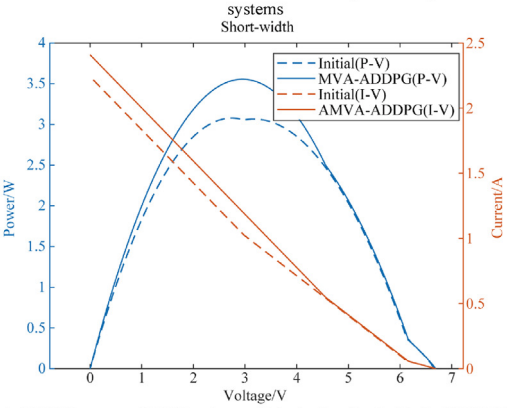

(c) *I-V/P-V* curves of TEG in short-width shading for 6×4 hybrid PV-TEG systems

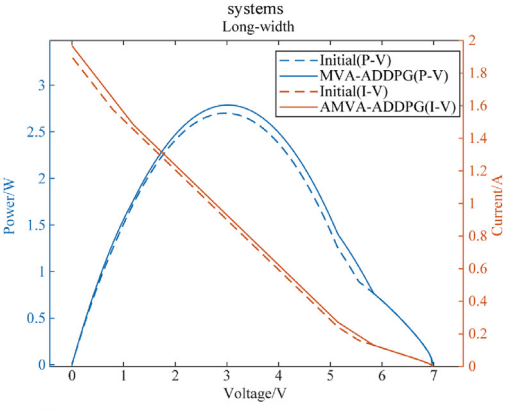

(d) *I-V/P-V* curves of TEG in long-width shading for 6×4 hybrid PV-TEG systems

Fig 7. *(continued)*

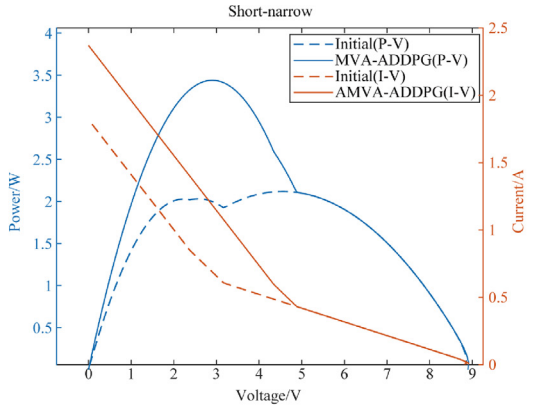

(e) *I-V/P-V* curves of TEG in short-narrow shading for 6×4 hybrid PV-TEG systems

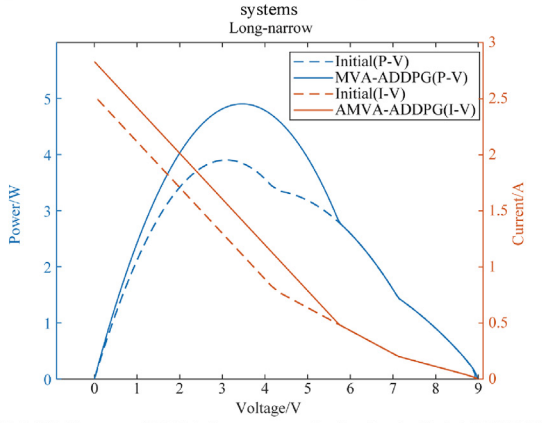

(f) *I-V/P-V* curves of TEG in long-narrow shading for 6×4 hybrid PV-TEG systems

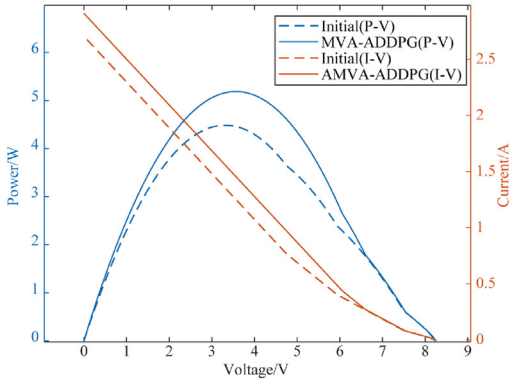

(g) *I-V/P-V* curves of TEG in diagonal shading for 6×4 hybrid PV-TEG systems

Fig 7. *(continued)*

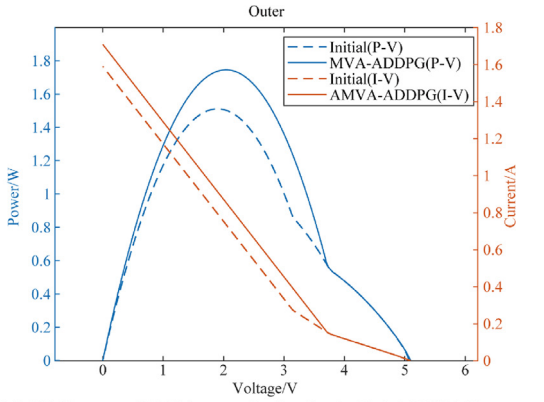

(h) *I-V/P-V* curves of TEG in outer shading for 6×4 hybrid PV-TEG systems

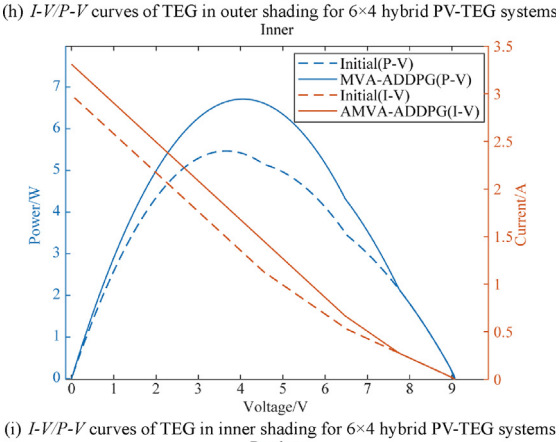

(i) *I-V/P-V* curves of TEG in inner shading for 6×4 hybrid PV-TEG systems

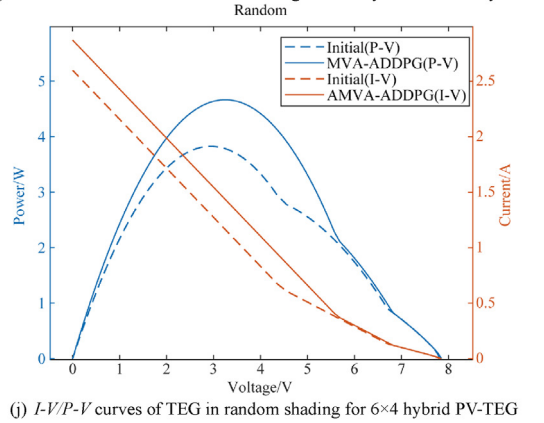

(j) *I-V/P-V* curves of TEG in random shading for 6×4 hybrid PV-TEG systems

Fig 7. *(continued)*

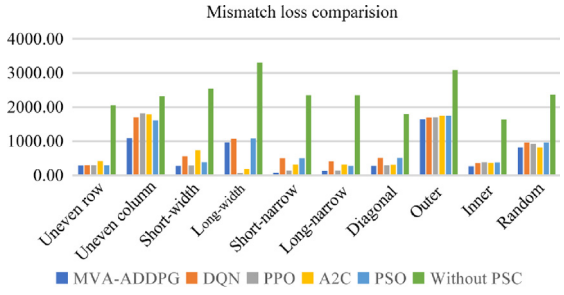

Fig. 8. Comparison of mismatch loss between four algorithmic cells after compensation and before compensation for 10 different PSC cases.

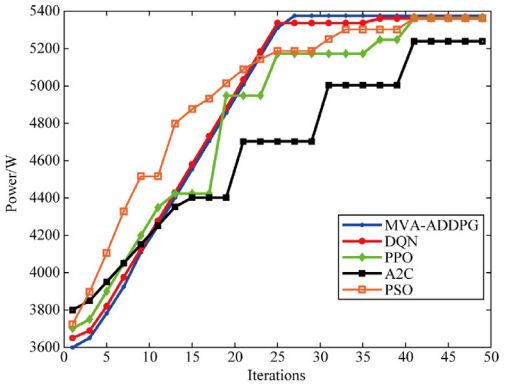

(a) Iteration curves of 4 algorithms in uneven row shading for 6×4 hybrid PV-TEG systems

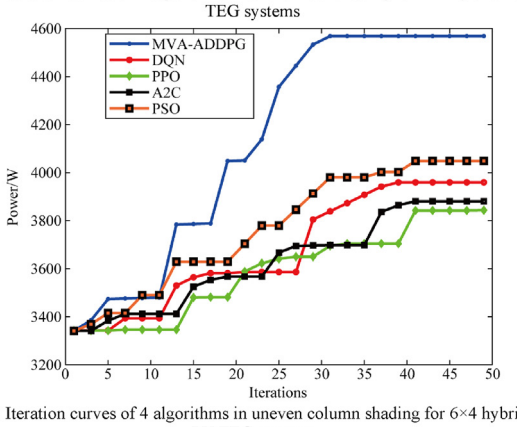

(b) Iteration curves of 4 algorithms in uneven column shading for 6×4 hybrid PV-TEG systems

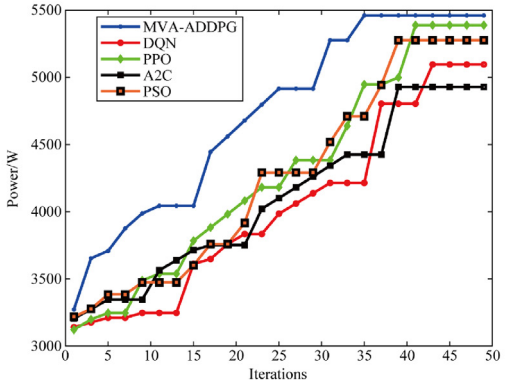

(c) Iteration curves of 4 algorithms in short-width shading for 6×4 hybrid PV-TEG systems

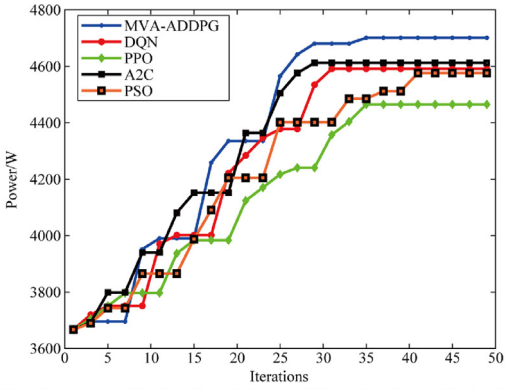

(d) Iteration curves of 4 algorithms in long-width shading for 6×4 hybrid PV-TEG systems

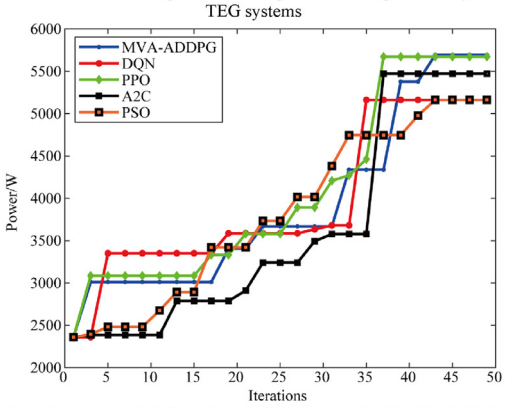

(e) Iteration curves of 4 algorithms in short-narrow shading for 6×4 hybrid PV-TEG systems

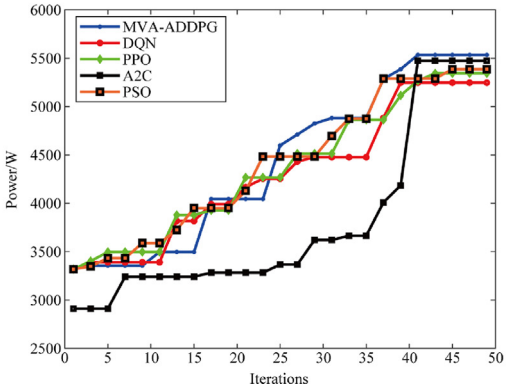

Fig 9. *(continued)*

Fig. 9. Iteration curves of the four algorithms at 6 × 4 different PSC.

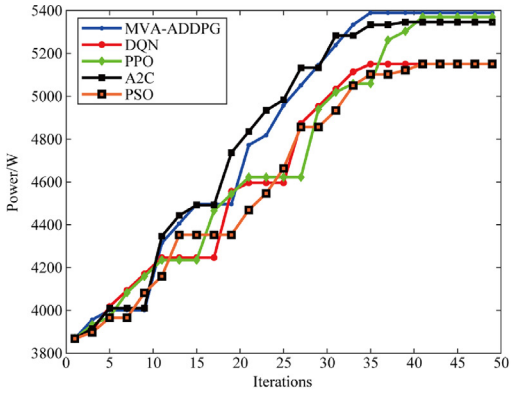

(g) Iteration curves of 4 algorithms in diagonal shading for 6×4 hybrid PV-TEG systems

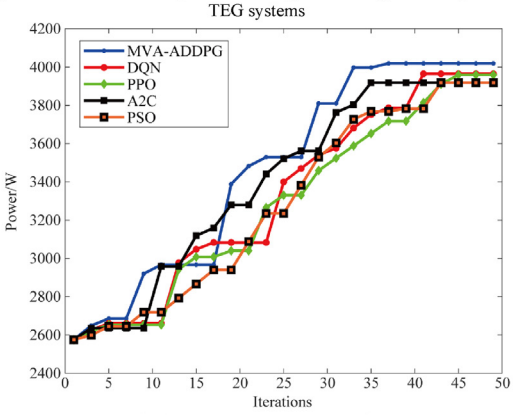

(h) Iteration curves of 4 algorithms in outer shading for 6×4 hybrid PV-TEG systems

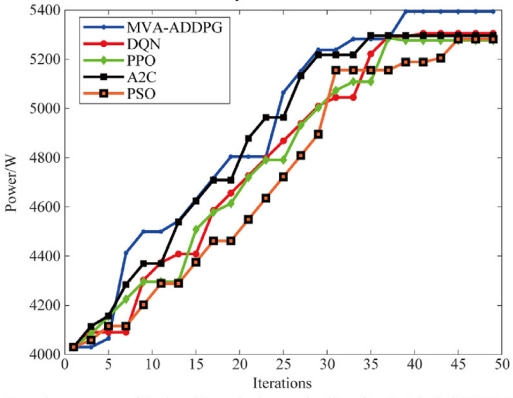

(i) Iteration curves of 4 algorithms in inner shading for 6×4 hybrid PV-TEG systems

Fig 9. *(continued)*

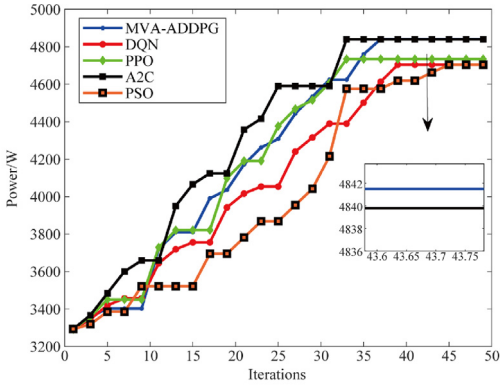

(j) Iteration curves of 4 algorithms in random shading for 6×4 hybrid PV-TEG systems

Fig 9. *(continued)*

self-awareness learning factor 2.0, social learning factor 2.0, particle number = 50) has a faster convergence speed in the early stage due to its heuristic search characteristics, but is prone to falling into local optima in the later stage. The final stable output power is 0.23% lower than MVA-DDPG, highlighting the global optimization advantages of MVA-DDPG momentum vector gradient and three action exploration strategy (Fig. 10).

4.2 Scenario II: 6 × 6 symmetrical square scale under ten standard shading test conditions

Based on the research in the previous section, this section investigates the performance of a symmetric 6 × 6 hybrid PV-TEG systems under ten practical PSC (Fig. B2). Detailed current compensation values for each row of 6 × 6 PV array across all ten shading patterns, including total current compensation for each algorithm, are presented in Table A5. Corresponding voltage compensation data for each column of 6 × 6 TEG array, along with the total voltage compensation for each shading scenario and algorithm, is summarized in Table A6. The system achieves a greater level of increase in the percentage of power enhancement and a greater reduction in the mismatch loss, as detailed in Tables A7 and A8. The system achieves a greater level of increase in the percentage of power enhancement and a greater reduction in the mismatch loss, as detailed in Table A8, Figs. 11 and 12 present the images of *P-V* and *I-V* of MVA-ADDPG for better analysis.

The case of 6 × 6 study demonstrates significant improvements in power optimization and reduction of mismatch loss. In scenarios where the base power is 4973.52 W, MVA-ADDPG-driven system achieves a maximum output power of 8080.08 W, resulting in a 27.38% power enhancement while maintaining a low mismatch loss of 20.75 W. In comparison, alternative configurations demonstrate a decline in performance; for instance, a com-

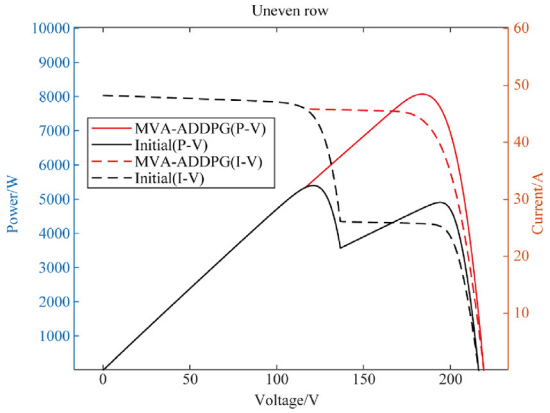

(a) *I-V*/*P-V* curves of PV in uneven row shading for 6×6 hybrid PV-TEG systems

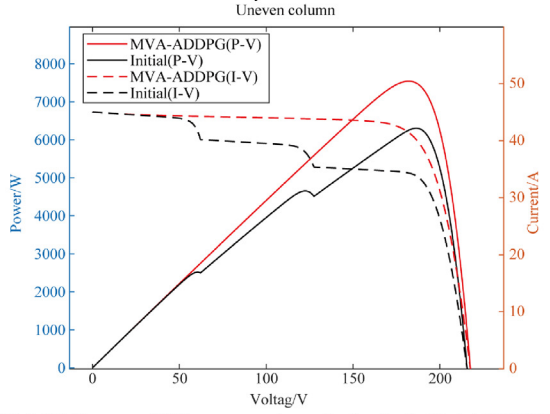

(b) *I-V*/*P-V* curves of PV in uneven column shading for 6×6 hybrid PV-TEG systems

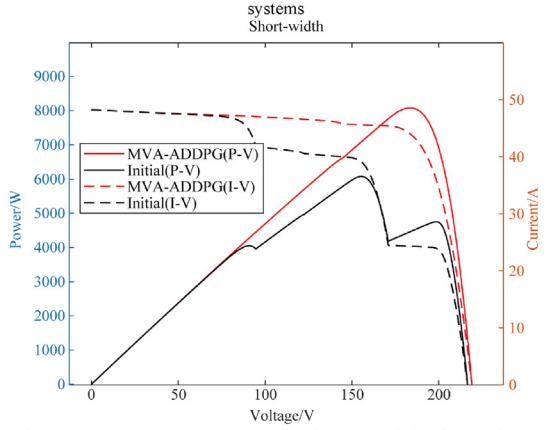

(c) *I-V*/*P-V* curves of PV in short-width shading for 6×6 hybrid PV-TEG systems

Fig. 10. *I-V* and *P-V* plots of the part of PV in 6 × 6 hybrid PV-TEG systems at ten irradiances under standard PSC.

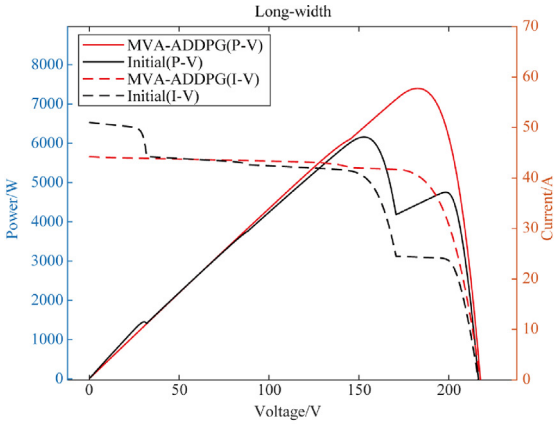

(d) *I-V*/*P-V* curves of PV in long-width shading for 6×6 hybrid PV-TEG systems

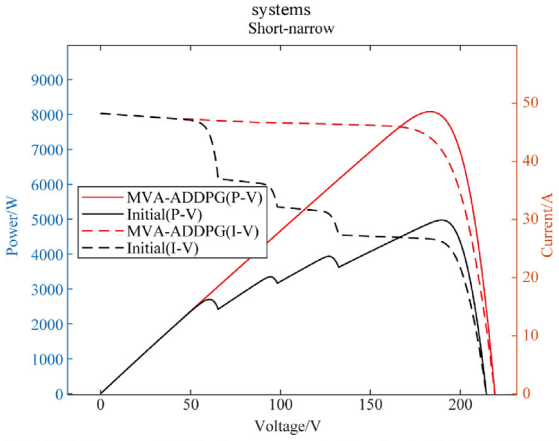

(e) *I-V*/*P-V* curves of PV in short-narrow shading for 6×6 hybrid PV-TEG systems

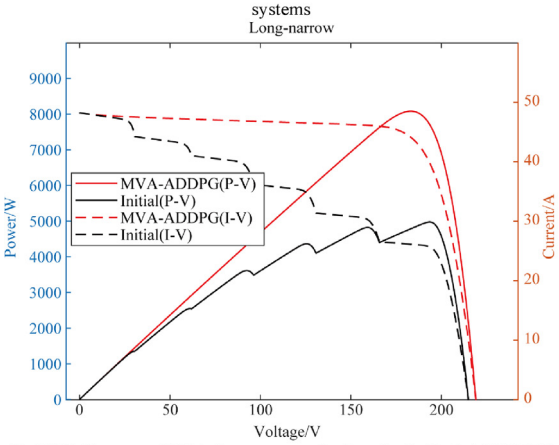

(f) *I-V*/*P-V* curves of PV in long-narrow shading for 6×6 hybrid PV-TEG systems

Fig 10. *(continued)*

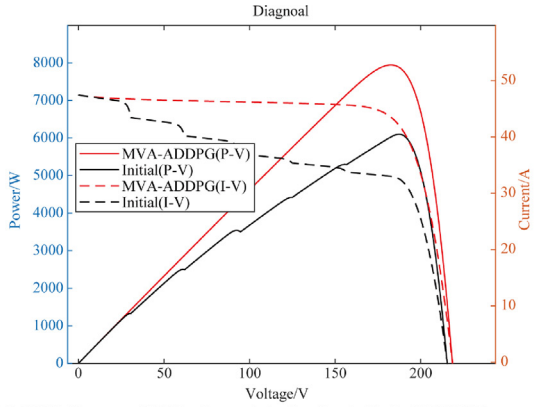

(g) *I-V*/*P-V* curves of PV in diagonal shading for 6×6 hybrid PV-TEG systems

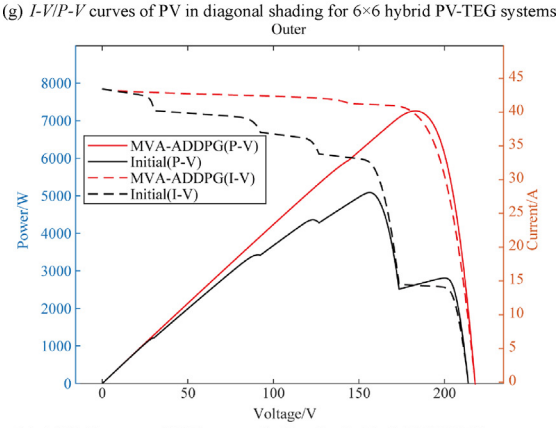

(h) *I-V*/*P-V* curves of PV in outer shading for 6×6 hybrid PV-TEG systems

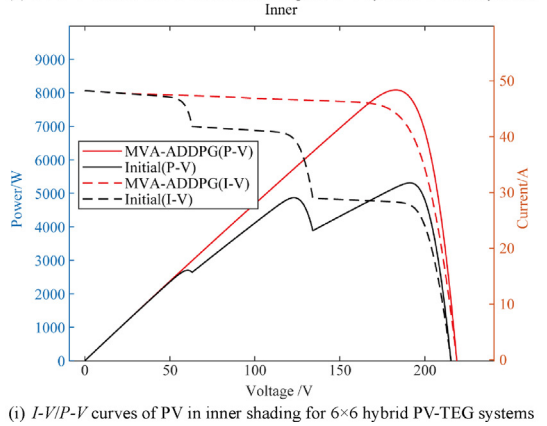

(i) *I-V*/*P-V* curves of PV in inner shading for 6×6 hybrid PV-TEG systems

Fig 10. *(continued)*

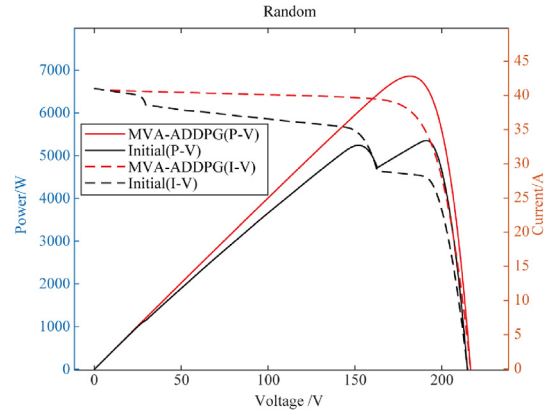

(j) *I-V*/*P-V* curves of PV in random shading for 6×6 hybrid PV-TEG systems

Fig 10. *(continued)*

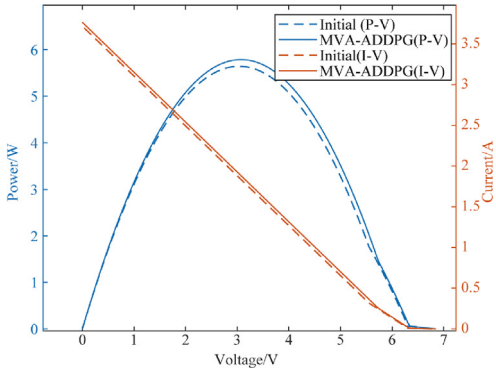

(a) *I-V*/*P-V* curves of TEG in uneven row shading for 6×6 hybrid PV-TEG systems

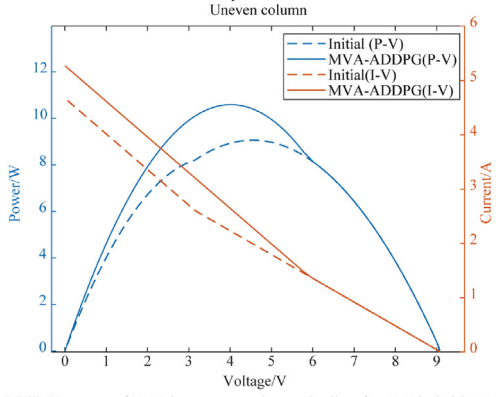

(b) *I-V*/*P-V* curves of TEG in uneven column shading for 6×6 hybrid PV-TEG systems

Fig. 11. *I-V* and *P-V* plots of the part of TEG in 6 × 6 hybrid PV-TEG systems at ten irradiances under standard PSC.

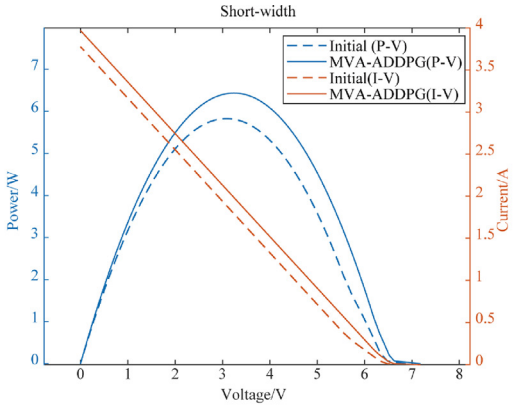

(c) *I-V/P-V* curves of TEG in short-width shading for 6×6 hybrid PV-TEG systems

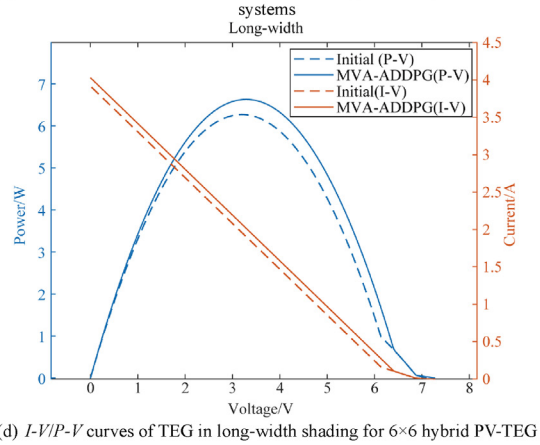

(d) *I-V/P-V* curves of TEG in long-width shading for 6×6 hybrid PV-TEG systems

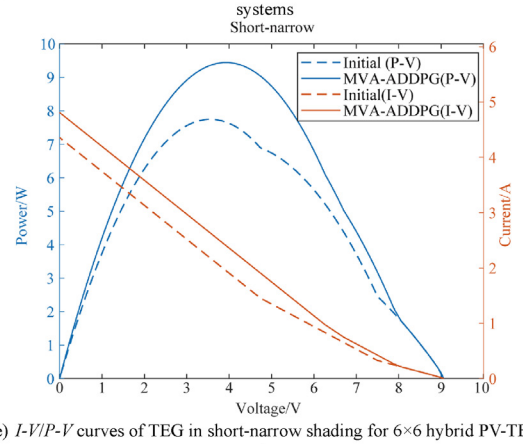

(e) *I-V/P-V* curves of TEG in short-narrow shading for 6×6 hybrid PV-TEG systems

Fig 11. *(continued)*

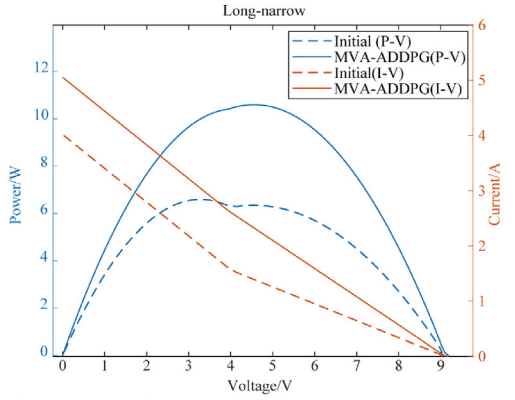

(f) *I-V/P-V* curves of TEG in long-narrow shading for 6×6 hybrid PV-TEG systems

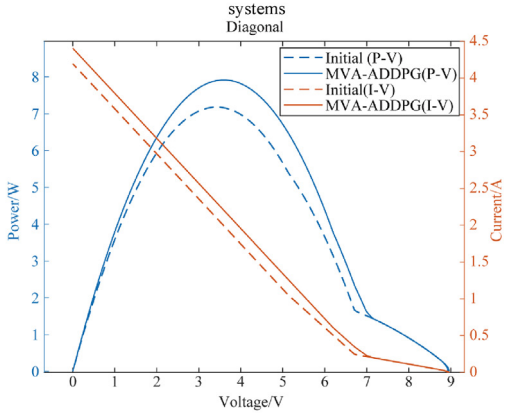

(g) *I-V/P-V* curves of TEG in diagonal shading for 6×6 hybrid PV-TEG systems

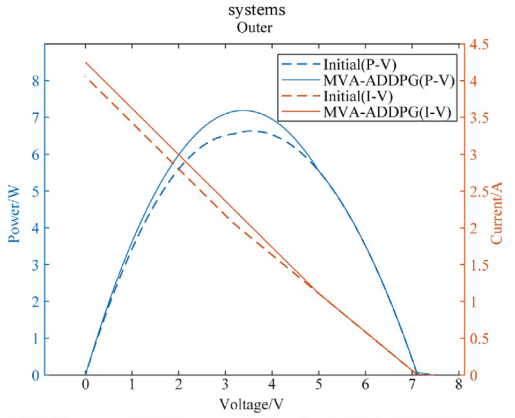

(h) *I-V/P-V* curves of TEG in outer shading for 6×6 hybrid PV-TEG systems

Fig 11. *(continued)*

parable base power case with 23% enhancement experiences a higher mismatch loss of 136.4 W, emphasizing the superior balance between efficiency and stability exhibited by MVA-ADDPG. It is also notable that in high-complexity layouts, the proposed method sustains a 6.77%-7.32% power improvement with controlled mismatch losses, outperforming benchmarks that show erratic efficiency trends. Figs. 12 and 13 illustrate, respectively, the mismatch loss summary and the iterative plots for 6 × 6 hybrid PV-TEG systems. As shown in Fig. 13 (a), PSO algorithm has an initial exploration efficiency advantage, but the local optimal problem results in a final maximum power that is still lower than MVA-DDPG, further verifying the superiority of MVA-DDPG method in balancing exploration and utilization in complex array topologies.

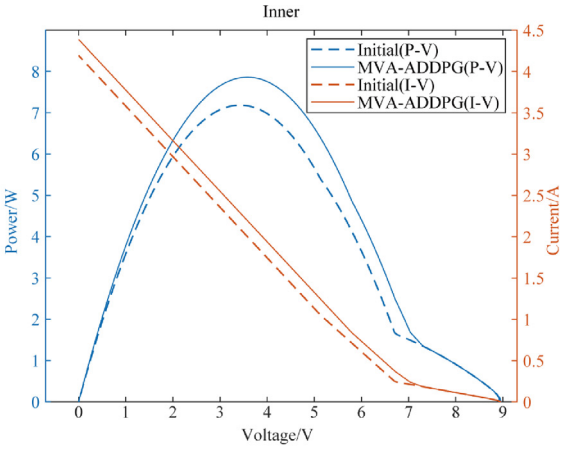

(i) *I-V/P-V* curves of TEG in inner shading for 6×6 hybrid PV-TEG systems

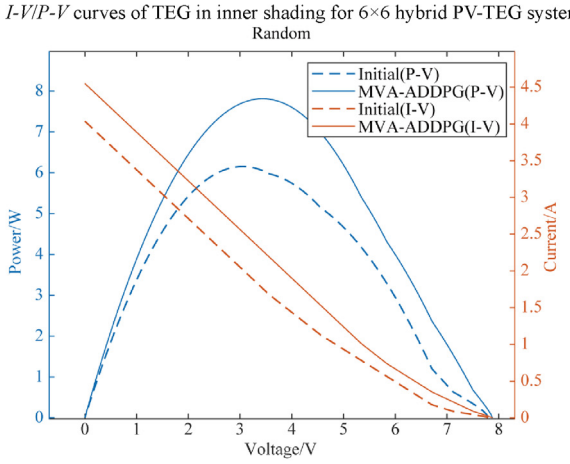

(j) *I-V/P-V* curves of TEG in random shading for 6×6 hybrid PV-TEG systems

Fig 11. *(continued)*

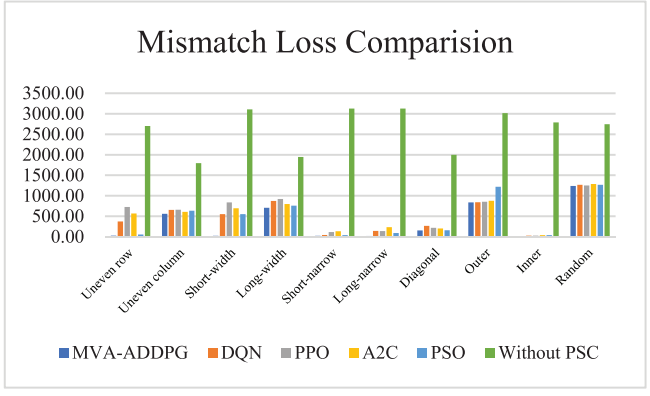

Fig. 12. Comparison of mismatch loss between four algorithmic cells after compensation and before compensation for 10 different PSC cases.

4.3 Ablation experiment

In 6 × 4 and 6 × 6 arrays (50 iterations), the three core modules of MVA-DDPG have significant effects: the momentum free variant (ABL1) has a 3%-5% slower convergence speed and 5 more stable iterations than the original algorithm; The power fluctuation of the single action variant (ABL2) reaches 2.1%, and the final stable power is 5.4% lower; The mid-term growth of single target variant (ABL3) slows down and stability decreases by 4.2%. This indicates that the synergistic effect of momentum acceleration, three action exploration, and dual objective reward module effectively improves the convergence efficiency, output power, and operational stability of the algorithm. As shown in Figs. 14 and 15.

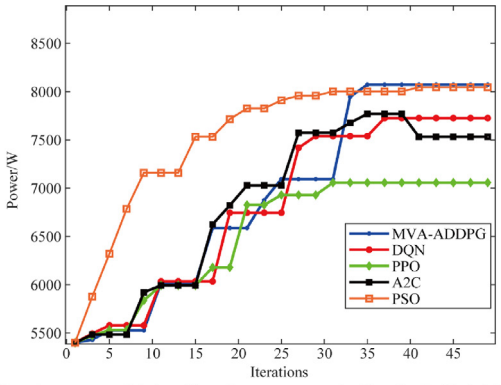

(a) Iteration curves of 4 algorithms in uneven row shading for 6×6 hybrid PV-TEG systems

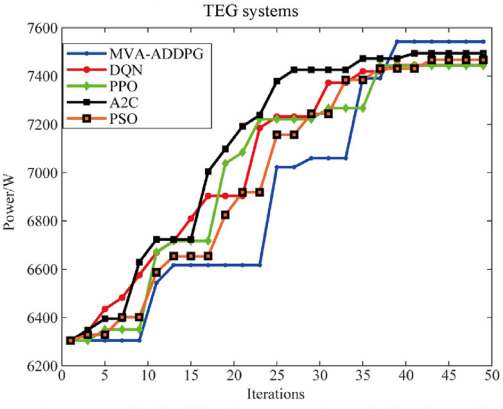

(b) Iteration curves of 4 algorithms in uneven column shading for 6×6 hybrid PV-TEG systems

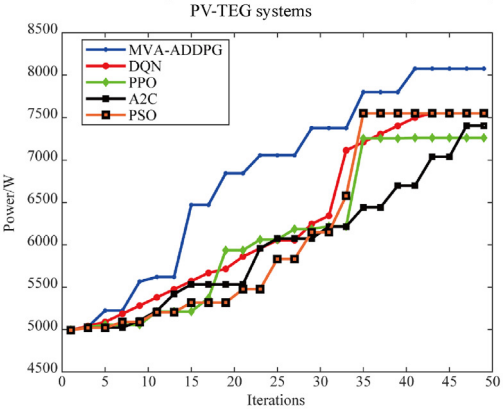

(c) Iteration curves of 4 algorithms in short-width shading for 6×6 hybrid PV-TEG systems

Fig. 13. Iteration curves of the four algorithms at 6 × 6 different PSC.

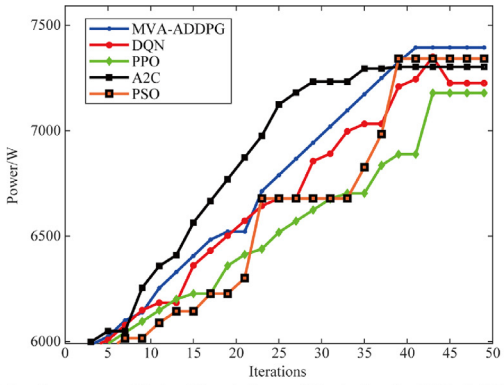

(d) Iteration curves of 4 algorithms in long-width shading for 6×6 hybrid PV-TEG systems

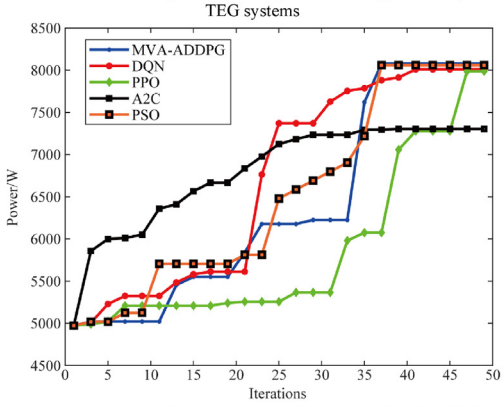

(e) Iteration curves of 4 algorithms in short-narrow shading for 6×6 hybrid PV-TEG systems

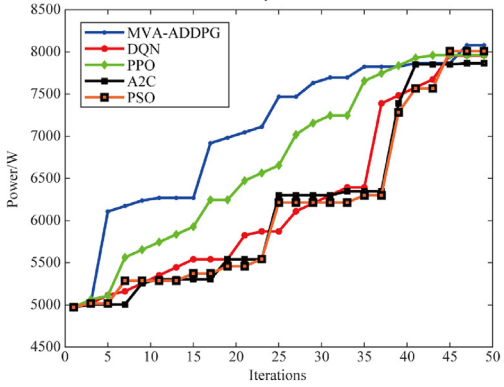

(f) Iteration curves of 4 algorithms in long-narrow shading for 6×6 hybrid PV-TEG systems

Fig 13. *(continued)*

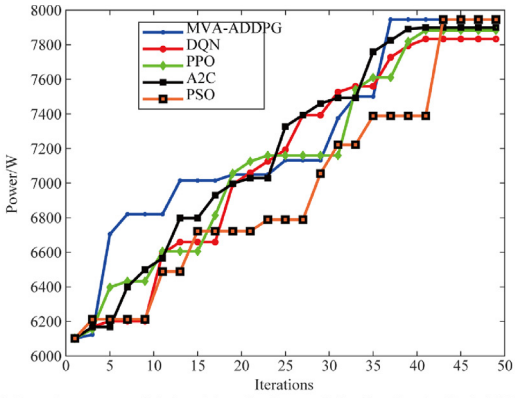

(g) Iteration curves of 4 algorithms in diagonal shading for 6×6 hybrid PV-TEG systems

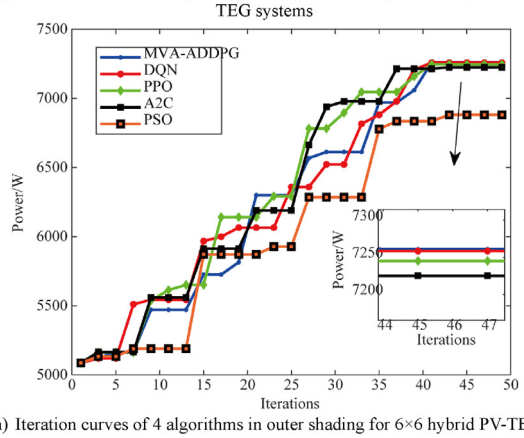

(h) Iteration curves of 4 algorithms in outer shading for 6×6 hybrid PV-TEG systems

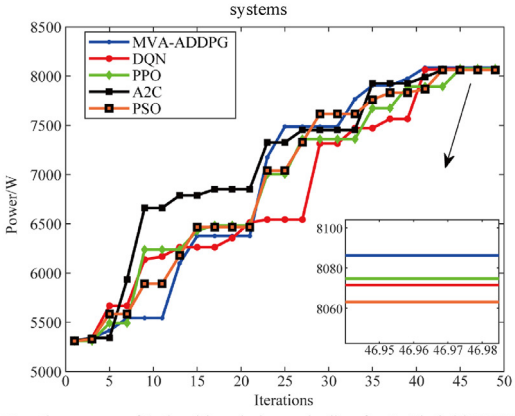

(i) Iteration curves of 4 algorithms in inner shading for 6×6 hybrid PV-TEG systems

Fig 13. *(continued)*

5 HIL validation

Hardware-in-the-loop (HIL) testing on RTLAB validates MVA-ADDPG in bridging simulations and hardware deployment. For scaling across 6 × 4 and 6 × 6 array configurations, dynamic hardware resource allocation is implemented—CPU cores are partitioned to handle array modelling. Measurement setup includes calibrated voltage/current sensors integrated with signal conditioning circuits to filter noise, and data transmission is achieved via Gigabit Ethernet (TCP/IP), ensuring synchronization between the control algorithm (running on an Intel Core i7-8650U 2.11 GHz CPU and 8 GB memory as well as an OP5700 simulator with dimensions of 48.3 cm (19 in.) × 28.0 cm (11 in.) × 14 cm (5.5 in.) and a weight of approximately 6.4 kg) and the simulated PV-TEG hardware. Meanwhile, the ODE4 solver with a fixed step size of 0.003 s is used to align with the real-time simulation requirements validated in similar PV array reconfiguration studies.

The algorithm adapts to varying system sizes (6 × 4/6 × 6 PV-TEG arrays) while preserving control

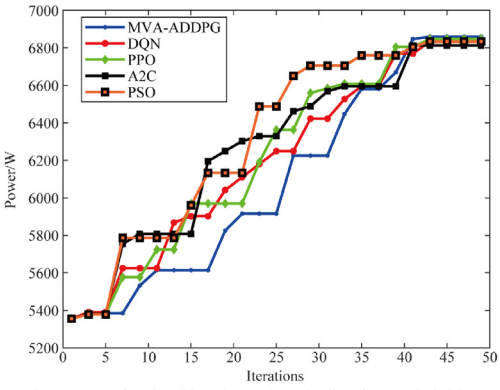

(j) Iteration curves of 4 algorithms in random shading for 6×6 hybrid PV-TEG systems

Fig 13. *(continued)*

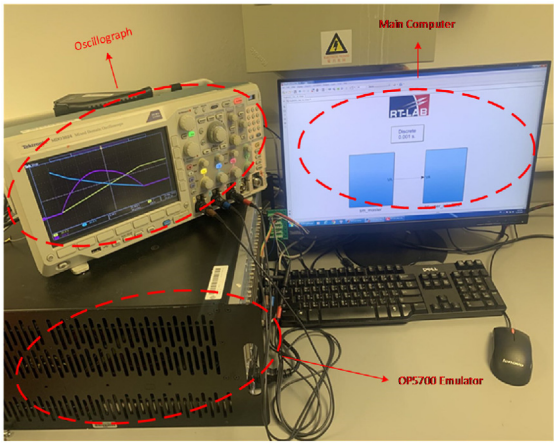

Fig. 16. HIL experiment hardware platform.

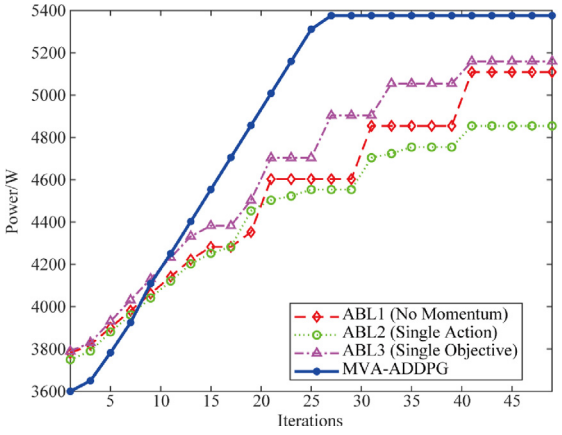

Fig. 14. Ablation experiment power-iteration curves of MVA-ADDPG under 6 × 4 uneven row.

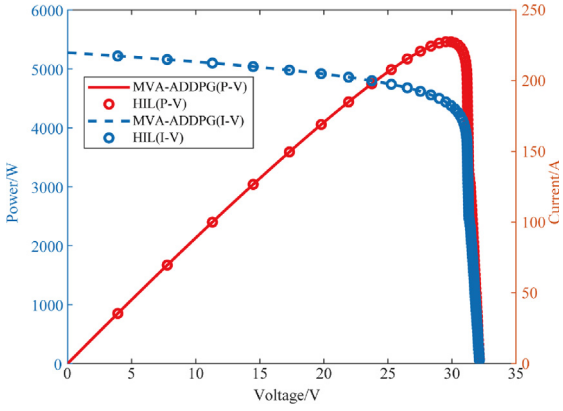

Fig. 17. HIL measured *P-V* and *I-V* curves of PV in 6 × 4 hybrid PV-TEG systems under uneven row shading.

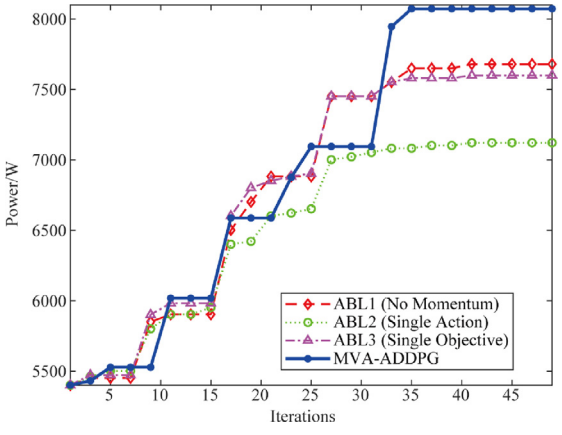

Fig. 15. Ablation experiment power-iteration curves of MVA-ADDPG under 6 × 6 uneven row.

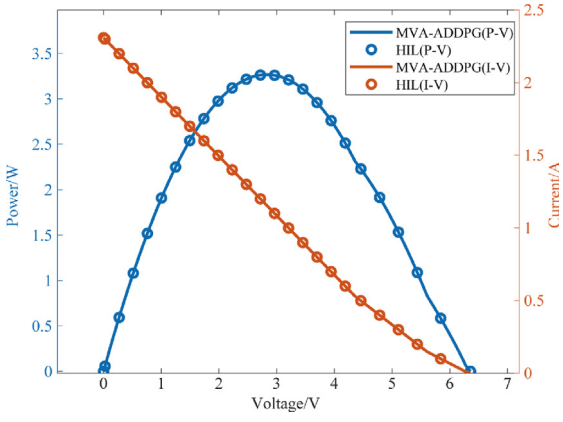

Fig. 18. HIL measured *P-V* and *I-V* curves of TEG in 6 × 4 hybrid PV-TEG systems under uneven row shading.

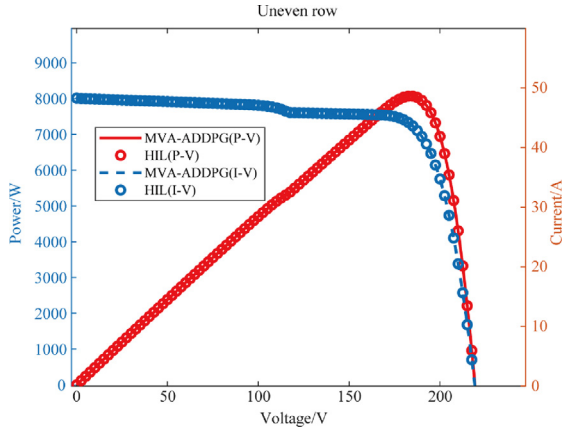

Fig. 19. HIL measured *P-V* and *I-V* curves of PV in 6 × 6 hybrid PV-TEG systems under uneven row shading.

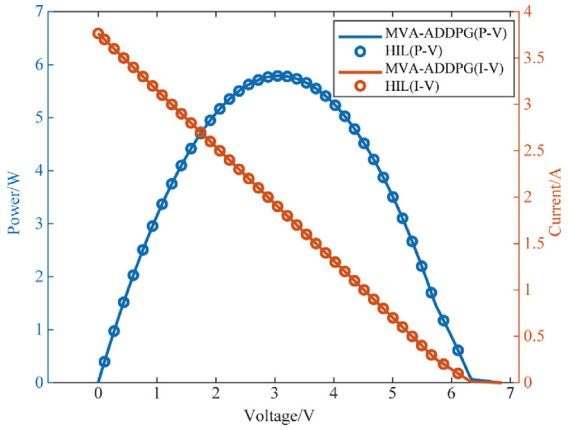

Fig. 20. HIL measured *P-V* and *I-V* curves of TEG in 6 × 6 hybrid PV-TEG systems under uneven row shading.

fidelity. Unlike conventional methods that struggle with hardware delays or shading complexity, MVA-ADDPG dynamically recalibrates compensation to align simulated and experimental results. Its architecture-independent design ensures consistent accuracy across topologies, balancing computational efficiency.

Figs. 15 and 16 demonstrate that, with MVA-ADDPG battery participation, there is a significant enhancement in power output and a dramatic reduction in mismatch losses.

For example, HIL-measured *P-V* and *I-V* curves under "Short-width" localized shading (Fig. 15(c)) quantitatively validate MVA-ADDPG's optimization capabilities. In the left *P-V* plot, MVA-ADDPG algorithm (red curve) achieves a flattened maximum power plateau between 15 and 20 V, sustaining 4900 W output with <2% ripple. Notably, MVA-ADDPG's curve converges to 96.3% of the theoretical maximum power point at 18.6 V, aligning with MATLAB/Simulink-predicted value. This contrast highlights the algorithm's optimization-maximizing current and voltage in various constraints while dynamically compensating for mismatches induced by temperature variation and multimodal situation.

Both plots exhibit <3% deviation between simulation-predicted inflection points (circled) and HIL-measured data-demonstrates its effectiveness in suppressing partial shading-induced multi-modal losses, indicative of great stability (Figs. 17–20).

6 Conclusions

This study proposes a unified control framework for hybrid PV-TEG systems operating under partial shading conditions (PSC), using MVA-ADDPG to improve the system performance. The proposed approach addresses key challenges in power mismatch and thermal instability by coordinating adaptive waste heat recovery and energy storage regulation.

MVA-ADDPG algorithm integrates momentum-accelerated policy gradients and a tri-action exploration–exploitation strategy to stabilize training dynamics and improve convergence under dynamic environmental conditions. This facilitates precise optimization of battery dispatch and thermal electric compensation, resulting in improved energy efficiency and system reliability.

Experimental results demonstrate that the proposed method achieves configuration-specific power gains-up to 46.62% improvement in 6 × 4 short-narrow arrays and 29.04% in 6 × 6 short-width setups-outperforming conventional RL algorithms such as DQN, PPO, and A2C. Maximum performance margins reached 39.4% (6 × 4 vs. DQN) and 14.2% (6 × 6 vs. PPO). Lyapunov-based stability analysis confirms asymptotic convergence $\left(\frac{dV}{dt} < 0\right)$, with mismatch losses reduced by 45.2% and compensation current totaling 1818.65 A. HIL validation demonstrates high fidelity to simulation results (<3% error), confirming the scalability and practical viability of the proposed solution.

Two main directions are envisioned for future research:

1) Future research will optimize PV-TEG topologies (e.g., SSPV-TEG, CPV-TEG) by integrating phase change materials to stabilize thermal gradients and enhance heat recovery, coupled with bifacial PV and sun-tracking for optothermal optimization. Multi-objective algorithms (e.g., genetic algorithms) will balance thermoelectric-photovoltaic parameters (Seebeck coefficient, efficiency decay) to mitigate electrical-thermal mismatches.
2) Building upon the current framework, future work will implement multi-physical field control in building-integrated microgrids by integrating PV-TEG systems with digital twins. A closed-loop maintenance framework will leverage real-time thermal stress/storage lifespan monitoring algorithms to optimize fault resilience and cost-efficiency.

CRediT authorship contribution statement

Lei Zhou: Writing – original draft. **Bo Yang:** Writing – review & editing. **Shuai Zhou:** Writing – review & editing. **Hongbiao Li:** Conceptualization. **Dengke Gao:** Formal analysis. **Tek Tjing Lie:** Supervision. **Lin Jiang:** Supervision.

Declaration of competing interest

The authors declare the following financial interests/personal relationships which may be considered as potential competing interests: Hongbiao Li and Dengke Gao are currently employed by Shanghai KeLiang Information Technology Company Ltd. The other authors declare that they have no known competing financial interests or personal relationships that could have appeared to influence the work reported in this paper.

Acknowledgments

This work is supported by National Natural Science Foundation of China (62263014), Yunnan Provincial Basic Research Project (202301AT070443, 202401AT070344).

Appendix A

Table A1
Compensation of dierent rows of cells in 6 × 4 PV array.

Algorithms	Type	Rows	Current compensation for each column (A)						
			Line 1	Line 2	Line 3	Line 4	Line 5	Line 6	Total current compensation
MVA-ADDPG	Uneven row		0	0	0	0	23.81	23.81	1460.46
	Uneven column		8.18	8.18	3.72	3.72	0	0	720.94
	Short-width		0	0	0	7.44	18.60	20.83	1182.23
	Long-width		0	0	2.23	2.23	4.46	18.30	697.37
	Short-narrow		0	0	13.99	13.99	18.66	18.66	1100.21
	Long-narrow		0	0.74	4.46	7.44	10.42	13.39	2234.58
	Diagonal		0	0.74	4.46	7.44	10.42	6.70	905.62
	Outer		2.23	2.23	0	0	14.58	13.89	901.20
	Inner		0	0	4.46	10.42	4.46	0	586.89
	Random		3.72	5.95	0	0	10.42	7.44	835.77
DQN	Uneven row		0.00	0.00	0.00	0.00	22.60	22.60	1500.00
	Uneven column		8.02	8.02	3.56	3.56	0.00	0.00	308.22
	Short-width		0.00	0.00	0.00	7.36	18.29	20.17	983.98
	Long-width		0.00	0.00	1.49	1.49	2.98	17.11	624.16
	Short-narrow		0.00	0.00	12.19	12.19	16.25	16.25	1731.92
	Long-narrow		0.00	0.67	4.02	6.70	9.37	12.05	990.84
	Diagonal		0.00	0.59	3.53	5.88	8.23	5.29	707.39
	Outer		1.49	1.49	0.00	0.00	13.39	13.39	857.37
	Inner		0.00	0.00	3.97	9.27	3.97	0.00	514.93
	Random		3.24	5.18	0.00	0.00	9.06	6.47	719.82
PPO	Uneven row		0.00	0.00	0.00	0.00	22.60	22.60	1449.76
	Uneven column		7.99	7.99	3.44	3.44	0.00	0.00	281.46
	Short-width		0.00	0.00	0.00	7.66	17.54	20.45	950.48
	Long-width		0.00	0.00	1.20	1.48	2.81	14.72	595.43
	Short-narrow		0.00	0.00	12.94	12.94	15.62	15.62	2341.60
	Long-narrow		0.00	0.83	5.00	8.33	11.67	15.00	1264.99
	Diagonal		0.00	0.73	4.37	7.29	10.21	6.56	885.88
	Outer		1.64	1.64	0.00	0.00	12.73	12.73	860.64
	Inner		0.00	0.00	3.84	8.97	3.84	0.00	496.75
	Random		3.33	5.33	0.00	0.00	9.33	6.67	742.37

Table A1 (*continued*)

Algorithms	Type	Rows	Current compensation for each column (A)						
			Line 1	Line 2	Line 3	Line 4	Line 5	Line 6	Total current compensation
A2C	Uneven row		0.00	0.00	0.00	0.00	25.03	25.03	1365.45
	Uneven column		8.11	8.11	3.59	3.59	0.00	0.00	0.00
	Short-width		0.00	0.00	0.00	7.66	18.41	20.68	720.94
	Long-width		0.00	0.00	1.44	1.48	2.51	16.05	308.22
	Short-narrow		0.00	0.00	13.39	13.39	17.86	17.86	281.46
	Long-narrow		0.00	0.72	4.32	7.19	10.07	12.95	294.51
	Diagonal		0.00	0.86	5.14	8.57	12.00	7.72	0.00
	Outer		1.38	1.38	0.00	0.00	12.45	12.45	1182.23
	Inner		0.00	0.00	3.93	9.17	3.93	0.00	983.98
	Random		3.79	6.07	0.00	0.00	10.62	7.59	1264.04
PSO	Uneven row		0.00	0.00	0.00	0.00	23.20	23.20	1450.21
	Uneven column		7.92	7.92	3.58	3.58	0.00	0.00	695.79
	Short-width		0.00	0.00	0.00	7.28	18.05	20.25	1167.29
	Long-width		0.00	0.00	2.15	2.15	4.28	17.65	688.71
	Short-narrow		0.00	0.00	13.65	13.65	18.00	18.00	1702.82
	Long-narrow		0.00	0.71	4.32	7.25	9.98	12.85	1427.30
	Diagonal		0.00	0.70	4.28	7.12	9.85	6.35	882.01
	Outer		2.15	2.15	0.00	0.00	13.95	13.25	869.69
	Inner		0.00	0.00	4.28	9.85	4.28	0.00	574.81
	Random		3.58	5.72	0.00	0.00	9.85	7.12	810.90

Table A2
Compensation of dierent columns of cells in 6 × 4 TEG array.

Algorithms	Type	Columns	Voltage compensation for each column (V)				
			Column 1	Column 2	Column 3	Column 4	Total voltage compensation
MVA-ADDPG	Uneven row		0.25	0.77	0.00	0.00	0.19
	Uneven column		8.18	8.18	3.72	3.72	0.51
	Short-width		1.99	3.01	0.00	0.00	0.34
	Long-width		0.00	0.00	0.29	1.18	0.08
	Short-narrow		0.00	1.97	1.70	1.72	0.98
	Long-narrow		0.00	0.00	1.57	1.61	0.85
	Diagonal		0.66	1.30	0.04	0.00	0.62
	Outer		0.57	0.00	0.00	0.56	1.55
	Inner		0.00	1.94	1.22	0.00	0.89
	Random		1.14	1.31	0.00	0.19	0.76
DQN	Uneven row		0.23	0.77	0.00	0.00	0.19
	Uneven column		1.58	2.85	0.00	0.00	0.51
	Short-width		0.00	1.58	0.03	0.03	0.34
	Long-width		0.00	0.00	0.29	1.07	0.08
	Short-narrow		0.00	2.03	1.77	1.79	1.04
	Long-narrow		0.00	0.00	1.43	1.56	0.85
	Diagonal		0.83	1.28	0.08	0.00	0.55
	Outer		0.57	0.00	0.00	0.56	1.55
	Inner		0.00	1.86	1.30	0.00	0.89
	Random		1.14	1.21	0.00	0.11	0.76

Table A2 (*continued*)

Algorithms	Type	Columns	Voltage compensation for each column (V)				
			Column 1	Column 2	Column 3	Column 4	Total voltage compensation
PPO	Uneven row		0.19	0.77	0.00	0.00	0.136
	Uneven column		1.51	2.85	0.00	0.00	0.51
	Short-width		0.00	1.54	0.15	0.15	0.34
	Long-width		0.00	0.00	0.29	0.86	0.08
	Short-narrow		0.00	1.84	1.62	1.54	0.92
	Long-narrow		0.00	0.00	1.52	1.66	0.77
	Diagonal		0.77	1.37	0.05	0.00	0.55
	Outer		0.59	0.00	0.00	0.54	1.55
	Inner		0.00	1.93	1.23	0.00	0.89
	Random		1.22	1.16	0.00	0.25	0.76
A2C	Uneven row		0.06	0.77	0.00	0.00	0.14
	Uneven column		1.03	2.84	0.00	0.00	0.59
	Short-width		0.00	1.56	0.15	0.13	0.34
	Long-width		0.00	0.00	0.29	0.39	0.08
	Short-narrow		0.00	2.01	1.63	1.55	0.86
	Long-narrow		0.72	1.28	0.01	0.00	0.77
	Diagonal		0.74	1.32	0.05	0.00	1.55
	Outer		0.46	0.00	0.00	0.48	0.55
	Inner		0.00	1.85	1.31	0.00	0.89
	Random		1.16	1.20	0.00	0.10	0.69
PSO	Uneven row		0.23	0.75	0.00	0.00	0.17
	Uneven column		7.92	7.92	3.58	3.58	0.49
	Short-width		1.92	2.93	0.00	0.00	0.32
	Long-width		0.00	0.00	0.27	1.12	0.06
	Short-narrow		0.00	1.91	1.65	1.67	0.94
	Long-narrow		0.00	0.00	1.51	1.55	0.81
	Diagonal		0.62	1.25	0.03	0.00	0.58
	Outer		0.53	0.00	0.00	0.52	1.48
	Inner		0.00	1.88	1.17	0.00	0.85
	Random		1.09	1.26	0.00	0.17	0.71

Table A3
Statistical tables of 6 × 4 asymmetrical array.

Type	Initial power (W)	Algorithms								
		MVA-ADDPG			DQN			PPO		
		P_n(W)	ΔP(W)	η(%)	P_n(W)	ΔP(W)	η(%)	P_n(W)	ΔP(W)	η(%)
Uneven row	3600.33	**3915.30**	**314.97**	**8.75**	3861.48	261.15	7.25	3913.31	312.98	8.69
Uneven column	3341.05	**3847.20**	**506.15**	**15.15**	3650.91	309.85	9.27	3560.37	219.32	6.56
Short-width	3122.49	**4205.98**	**1083.49**	**34.70**	4111.36	988.86	31.67	4196.79	1074.30	34.41
Long-width	3667.13	**4003.87**	**336.75**	**9.18**	3967.07	299.95	8.18	3869.62	202.49	5.52
Short-narrow	2359.83	**3460.04**	**1100.21**	**46.62**	3431.87	1072.04	45.43	3332.20	972.37	41.20
Long-narrow	3319.01	**4276.04**	**957.02**	**28.83**	4256.44	937.42	28.24	4253.38	934.36	28.15
Diagonal	3868.20	**4484.37**	**616.17**	**15.93**	4443.12	574.92	14.86	4484.09	615.89	15.92
Outer	2575.34	**3117.86**	**542.52**	**21.07**	3107.52	532.18	20.66	3098.32	522.98	20.31
Inner	4029.97	**4807.03**	**777.06**	**19.28**	4790.46	760.49	18.87	4780.29	750.32	18.62
Random	3293.15	**4005.74**	**712.60**	**21.64**	3984.79	691.65	21.00	3992.24	699.10	21.23

Table A4
Statistical tables of 6 × 4 asymmetrical array.

Type	Initial power (W)	Algorithms					
		A2C			PSO		
		P_n(W)	ΔP(W)	η(%)	P_n(W)	ΔP(W)	η(%)
Uneven row	3600.33	3874.12	273.80	7.60	3912.80	312.47	8.68
Uneven column	3341.05	3585.73	244.67	7.32	3840.50	499.45	14.95
Short-width	3122.49	4029.14	906.65	29.04	4198.20	1075.71	34.45
Long-width	3667.13	3974.80	307.67	8.39	3999.20	332.07	9.05
Short-narrow	2359.83	3453.95	1094.12	46.36	3458.50	1098.67	46.56
Long-narrow	3319.01	4273.47	954.46	28.76	4270.80	951.79	28.68
Diagonal	3868.20	4463.16	594.96	15.38	4478.60	610.40	15.78
Outer	2575.34	3092.03	516.69	20.06	3112.60	537.26	20.86
Inner	4029.97	4787.31	757.34	18.79	4799.50	769.53	19.09
Random	3293.15	4005.29	712.14	21.62	3998.40	705.25	21.42

Table A5
Compensation of dierent rows of cells in 6 × 6 PV array.

Algorithms	Type Rows	Current compensation for each column (A)						
		Line 1	Line 2	Line 3	Line 4	Line 5	Line 6	Total current compensation
MVA-ADDPG	Uneven row	0.00	0.00	0.00	0.00	29.76	29.76	1818.65
	Uneven column	8.93	8.93	4.46	4.46	0.00	0.00	811.63
	Short-width	0.00	0.00	0.00	5.95	16.37	31.25	1633.73
	Long-width	0.00	0.00	1.49	1.49	2.98	27.53	1012.59
	Short-narrow	0.00	0.00	10.42	14.88	19.34	19.34	1953.26
	Long-narrow	0.00	3.72	6.70	11.16	15.62	20.09	1745.81
	Diagonal	0.00	3.72	6.70	9.67	11.16	12.65	1334.74
	Outer	0.00	0.00	1.49	1.49	17.86	17.86	1447.73
	Inner	0.00	5.95	17.86	17.86	5.95	0.00	1450.08
	Random	0.00	2.23	4.46	2.98	11.16	3.72	743.15
DQN	Uneven row	0.00	0.00	0.00	0.00	26.76	26.76	1596.14
	Uneven column	7.66	8.27	4.17	3.98	0.00	0.00	725.10
	Short-width	0.00	0.00	0.00	7.05	17.45	33.31	1710.28
	Long-width	0.00	0.00	1.47	1.43	2.95	26.42	1222.62
	Short-narrow	0.00	0.00	10.31	14.73	19.15	19.15	1931.82
	Long-narrow	0.00	3.49	6.30	10.50	14.70	18.91	1634.65
	Diagonal	0.00	3.65	5.53	9.48	9.54	12.75	1246.05
	Outer	0.00	0.00	1.48	1.48	17.64	17.64	1450.73
	Inner	0.00	5.80	17.69	17.79	5.90	0.00	1435.96
	Random	0.00	2.06	4.12	2.75	11.31	3.44	718.26
PPO	Uneven row	0.00	0.00	0.00	0.00	24.33	24.33	1438.00
	Uneven column	7.51	8.10	4.08	4.53	0.00	0.00	729.22
	Short-width	0.00	0.00	0.00	5.99	14.83	28.31	1526.65
	Long-width	0.00	0.00	1.47	1.43	2.80	27.92	915.80
	Short-narrow	0.00	0.00	10.00	14.28	18.57	18.57	1867.38
	Long-narrow	0.00	3.50	6.31	10.51	14.71	18.92	1636.23
	Diagonal	0.00	4.09	7.37	10.64	10.32	10.99	1322.11
	Outer	0.00	0.00	1.42	1.42	17.67	17.67	1460.00
	Inner	0.00	5.81	17.82	17.82	5.81	0.00	1438.70
	Random	0.00	2.10	4.20	2.80	11.51	3.50	732.82

Table A5 (*continued*)

Algorithms	Type	Rows	Current compensation for each column (A)						
			Line 1	Line 2	Line 3	Line 4	Line 5	Line 6	Total current compensation
A2C	Uneven row		0.00	0.00	0.00	0.00	25.38	25.38	1505.15
	Uneven column		8.02	8.02	5.42	4.46	0.00	0.00	783.07
	Short-width		0.00	0.00	0.00	5.85	14.47	27.63	1598.40
	Long-width		0.00	0.00	1.43	1.43	2.74	27.30	1088.97
	Short-narrow		0.00	0.00	9.90	14.14	18.38	18.38	1847.14
	Long-narrow		0.00	3.35	6.02	10.04	14.05	18.07	1558.90
	Diagonal		0.00	3.68	6.63	9.67	11.05	11.68	1296.52
	Outer		0.00	0.00	1.41	1.41	17.93	17.93	1480.73
	Inner		0.00	5.94	17.71	17.41	5.97	0.00	1429.02
	Random		0.00	2.00	4.00	2.67	11.01	3.34	696.74
PSO	Uneven row		0.00	0.00	0.00	0.00	29.20	29.20	1792.31
	Uneven column		8.72	8.72	4.32	4.32	0.00	0.00	798.39
	Short-width		0.00	0.00	0.00	5.78	15.85	30.35	1557.10
	Long-width		0.00	0.00	1.43	1.43	2.88	26.65	995.31
	Short-narrow		0.00	0.00	10.15	14.45	18.75	18.75	1936.17
	Long-narrow		0.00	3.60	6.45	10.75	15.05	19.45	1736.89
	Diagonal		0.00	3.60	6.45	9.35	10.75	12.15	1343.80
	Outer		0.00	0.00	1.39	1.39	17.25	17.25	1395.20
	Inner		0.00	5.78	17.25	17.25	5.78	0.00	1432.24
	Random		0.00	2.08	4.15	2.72	10.65	3.32	718.46

Table A6
Compensation of dierent columns of cells in 6 × 6 TEG array.

Algorithms	Type	Columns	Voltage compensation for each column (V)						
			Column 1	Column 2	Column 3	Column 4	Column 5	Column 6	Total voltage compensation
MVA-ADDPG	Uneven row		1.33	1.94	1.17	1.17	0.00	0.00	1.81
	Uneven column		2.62	2.86	0.00	0.00	0.00	0.00	0.85
	Short-width		0.81	0.81	0.99	0.99	0.00	0.00	1.18
	Long-width		0.96	2.45	2.15	1.57	0.78	0.00	0.33
	Short-narrow		0.97	2.54	2.15	1.57	0.79	0.00	1.18
	Long-narrow		0.00	0.00	0.00	5.08	4.12	4.92	2.42
	Diagonal		0.97	2.54	2.15	1.57	0.79	0.00	2.49
	Outer		1.30	0.00	0.00	0.00	0.00	1.48	3.13
	Inner		0.00	2.76	2.37	2.37	3.90	0.00	0.81
	Random		1.41	1.80	0.00	0.79	0.43	0.76	1.25
DQN	Uneven row		1.15	1.94	1.17	1.17	0.00	0.00	1.37
	Uneven column		2.59	2.89	0.00	0.00	0.00	0.00	0.85
	Short-width		0.80	0.81	0.99	0.99	0.00	0.00	1.17
	Long-width		0.89	2.54	2.15	1.57	0.77	0.89	0.31
	Short-narrow		0.96	2.45	2.15	1.57	0.78	0.00	1.18
	Long-narrow		0.00	0.00	0.00	4.98	3.11	4.88	2.42
	Diagonal		0.96	2.45	2.15	1.57	0.78	0.00	2.49
	Outer		1.30	0.00	0.00	0.00	0.00	1.44	2.96
	Inner		0.00	2.82	2.36	2.37	3.38	0.00	0.79
	Random		1.27	1.79	0.00	0.79	0.91	0.83	1.22

Table A6 (*continued*)

Algorithms	Type	Columns	Voltage compensation for each column (V)						
			Column 1	Column 2	Column 3	Column 4	Column 5	Column 6	Total voltage compensation
PPO	Uneven row		1.20	1.87	1.17	1.17	0.00	0.00	1.43
	Uneven column		2.69	2.79	0.00	0.00	0.00	0.00	0.77
	Short-width		0.79	0.81	0.99	0.99	0.00	0.00	1.17
	Long-width		0.87	2.54	2.15	1.57	0.79	0.00	0.22
	Short-narrow		0.89	2.54	2.15	1.57	0.77	0.00	1.17
	Long-narrow		0.00	0.00	0.00	5.08	4.30	2.64	2.41
	Diagonal		0.89	2.54	2.15	1.57	0.77	0.00	2.44
	Outer		1.30	0.00	0.00	0.00	0.00	1.36	2.87
	Inner		0.00	2.79	2.37	2.37	3.55	0.00	0.74
	Random		1.42	1.94	0.00	0.79	1.07	0.76	1.16
A2C	Uneven row		1.44	1.94	1.17	1.17	0.00	0.00	1.31
	Uneven column		2.62	2.84	0.00	0.00	0.00	0.00	0.85
	Short-width		0.69	0.81	0.99	0.99	0.00	0.00	1.13
	Long-width		0.85	2.51	2.15	1.57	0.77	0.00	0.17
	Short-narrow		0.87	2.54	2.15	1.57	0.79	0.00	1.13
	Long-narrow		0.00	0.00	0.00	5.08	2.44	4.83	2.41
	Diagonal		0.87	2.54	2.15	1.57	0.79	0.00	2.44
	Outer		1.30	0.00	0.00	0.00	0.00	1.36	2.87
	Inner		0.00	2.98	2.37	2.37	2.93	0.00	0.78
	Random		1.44	1.99	0.00	0.78	0.56	0.38	1.10
PSO	Uneven row		1.28	1.89	1.13	1.13	0.00	0.00	1.76
	Uneven column		2.56	2.80	0.00	0.00	0.00	0.00	0.82
	Short-width		0.77	0.77	0.95	0.95	0.00	0.00	1.13
	Long-width		0.91	2.39	2.10	1.53	0.74	0.00	0.31
	Short-narrow		0.92	2.48	2.10	1.53	0.75	0.00	1.13
	Long-narrow		0.00	0.00	0.00	4.98	3.98	4.78	2.37
	Diagonal		0.92	2.48	2.10	1.53	0.75	0.00	2.44
	Outer		1.25	0.00	0.00	0.00	0.00	1.42	2.98
	Inner		0.00	2.70	2.32	2.32	3.82	0.00	0.78

Table A7
Statistical tables of 6 × 6 asymmetrical array.

Type	Initial power (W)	Algorithms								
		MVA-ADDPG			DQN			PPO		
		P_n(W)	ΔP(W)	η(%)	P_n(W)	ΔP(W)	η(%)	P_n(W)	ΔP(W)	η(%)
Uneven row	5400.59	**6254.06**	**853.48**	**15.80**	6254.06	853.48	15.80	6254.06	853.48	15.80
Uneven column	6304.43	**6731.06**	**426.64**	**6.77**	6731.06	426.64	6.77	6731.06	426.64	6.77
Short-width	4993.77	**6443.77**	**1450.00**	**29.04**	6443.77	1450.00	29.04	6443.77	1450.00	29.04
Long-width	5946.80	**6382.14**	**435.34**	**7.32**	6382.14	435.34	7.32	6382.14	435.34	7.32
Short-narrow	4973.52	**6125.25**	**1151.73**	**23.16**	6125.25	1151.73	23.16	6125.25	1151.73	23.16
Long-narrow	4972.76	**6334.27**	**1361.50**	**27.38**	6334.27	1361.50	27.38	6334.27	1361.50	27.38
Diagonal	6102.14	**6611.26**	**509.12**	**8.34**	6611.26	509.12	8.34	6611.26	509.12	8.34
Outer	5085.88	**5813.30**	**727.42**	**14.30**	5813.30	727.42	14.30	5813.30	727.42	14.30
Inner	5310.88	**6636.16**	**1325.27**	**24.95**	6636.16	1325.27	24.95	6636.16	1325.27	24.95
Random	5355.57	**6117.19**	**761.62**	**14.22**	6117.19	761.62	14.22	6117.19	761.62	14.22

Table A8
Statistical tables of 6 × 6 asymmetrical array.

Type	Initial power (W)	Algorithms					
		A2C			PSO		
		P_n(W)	P_n(W)	P_n(W)	P_n(W)	ΔP(W)	η(%)
Uneven row	5400.59	6026.74	626.15	11.59	6249.80	849.21	15.72
Uneven column	6304.43	6711.52	407.09	6.46	6723.60	419.17	6.65
Short-width	4993.77	5806.39	812.62	16.27	6432.50	1438.73	28.81
Long-width	5946.80	5679.15	267.64	4.50	6378.40	431.60	7.26
Short-narrow	4973.52	6117.30	1143.78	23.00	6122.10	1148.58	23.10
Long-narrow	4972.76	6307.09	1334.33	26.83	6326.90	1354.14	27.23
Diagonal	6102.14	6603.16	501.02	8.21	6607.50	505.36	8.28
Outer	5085.88	5744.27	658.39	12.94	5802.40	716.52	14.09
Inner	5310.88	6634.04	1323.15	24.91	6632.40	1321.52	24.88
Random	5355.57	6116.15	760.59	14.20	6112.30	756.73	14.13

Appendix B

Fig. B1. Table of 10 irradiances for 6 × 4 hybrid PV-TEG systems.

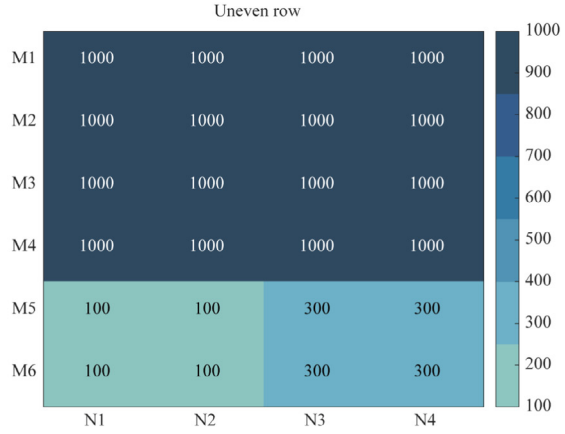

(a) Irradiance distribution of uneven row shading for 6×4 hybrid PV-TEG systems

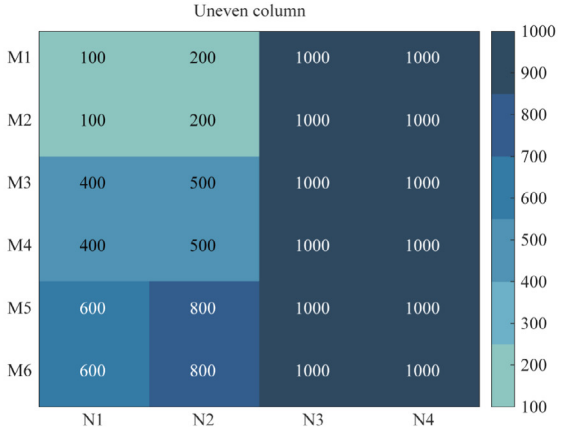

(b) Irradiance distribution of uneven column shading for 6×4 hybrid PV-TEG systems

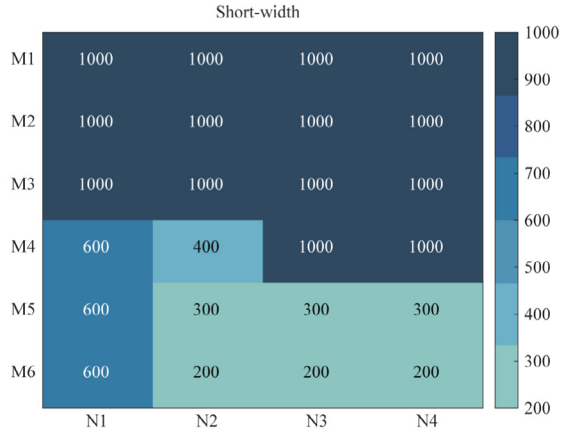

(c) Irradiance distribution of short-width shading for 6×4 hybrid PV-TEG systems

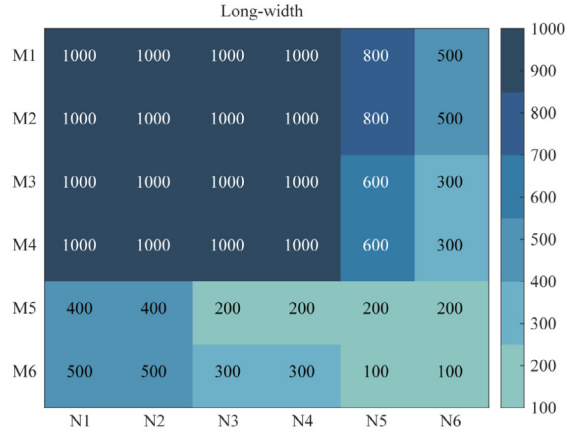

(d) Irradiance distribution of long-width shading for 6×4 hybrid PV-TEG systems

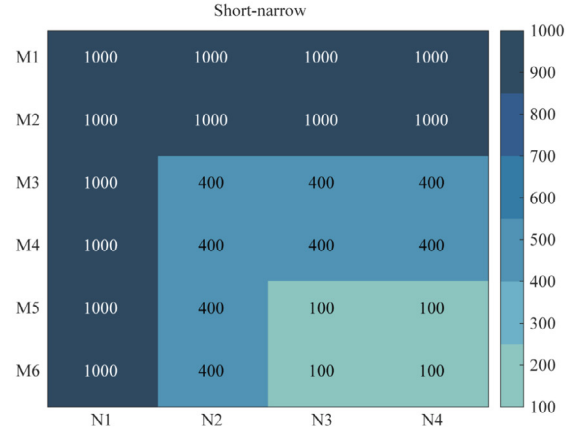

(e) Irradiance distribution of short-narrow shading for 6×4 hybrid PV-TEG systems

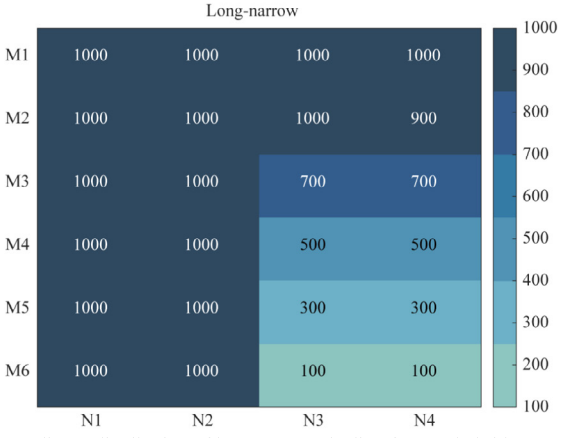

(f) Irradiance distribution of long-narrow shading for 6×4 hybrid PV-TEG systems

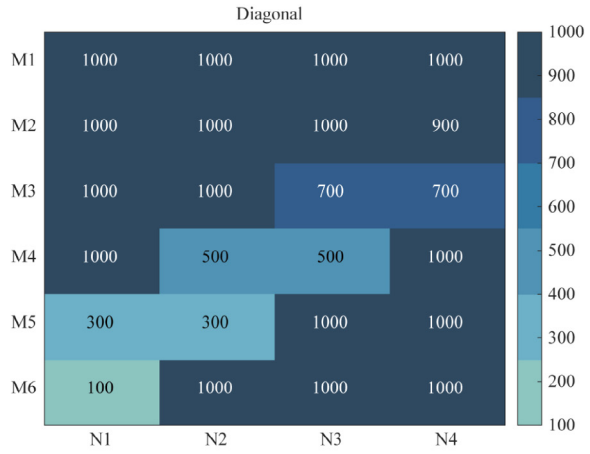

(g) Irradiance distribution of diagonal shading for 6×4 hybrid PV-TEG systems

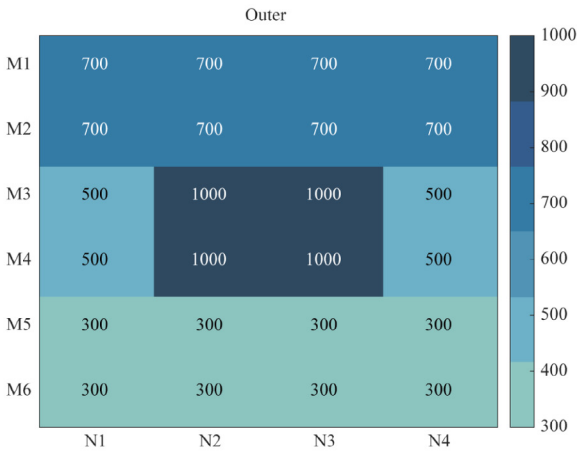

(h) Irradiance distribution of outer shading for 6×4 hybrid PV-TEG systems

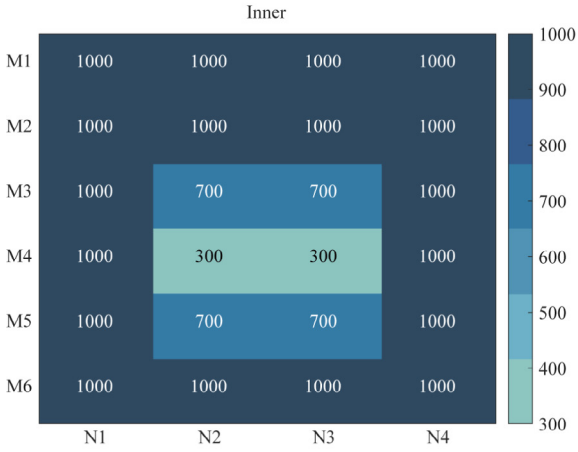

(i) Irradiance distribution of inner shading for 6×4 hybrid PV-TEG systems

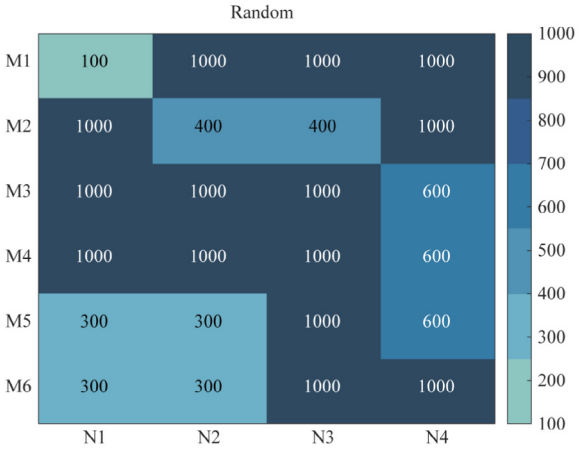

(j) Irradiance distribution of random shading for 6×4 hybrid PV-TEG systems

Fig. B2. Table of 10 irradiances for 6 × 6 hybrid PV-TEG systems.

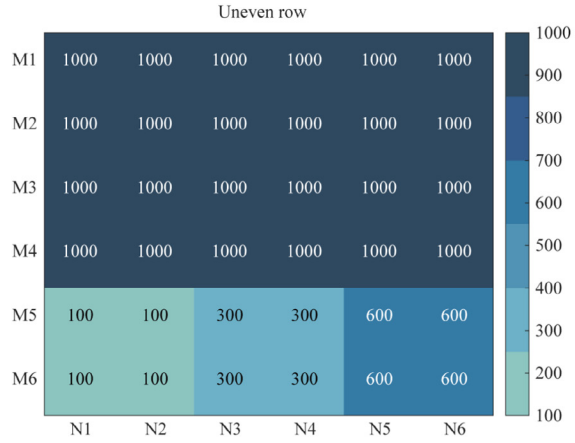

(a) Irradiance distribution of uneven row shading for 6×6 hybrid PV-TEG systems

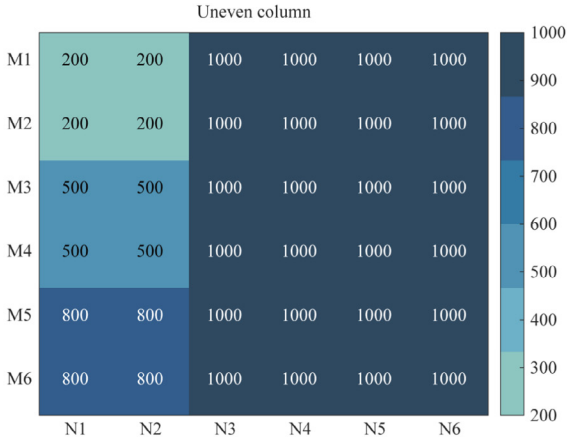

(b) Irradiance distribution of uneven column shading for 6×6 hybrid PV-TEG systems

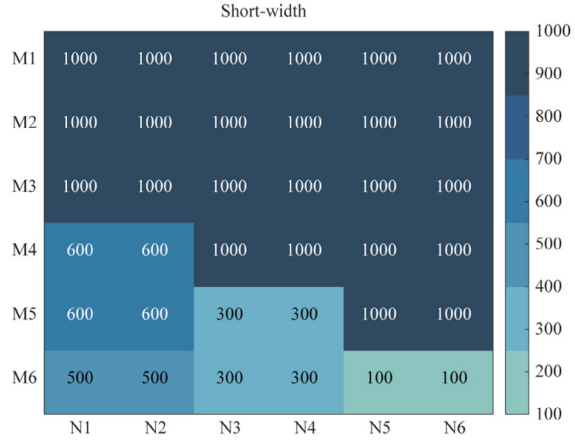

(c) Irradiance distribution of short-width shading for 6×6 hybrid PV-TEG systems

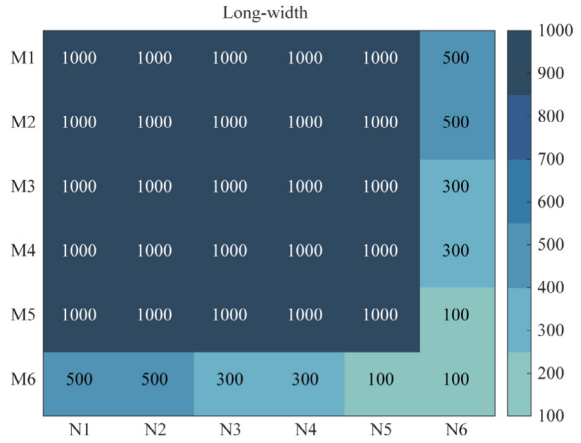

(d) Irradiance distribution of long-width shading for 6×6 hybrid PV-TEG systems

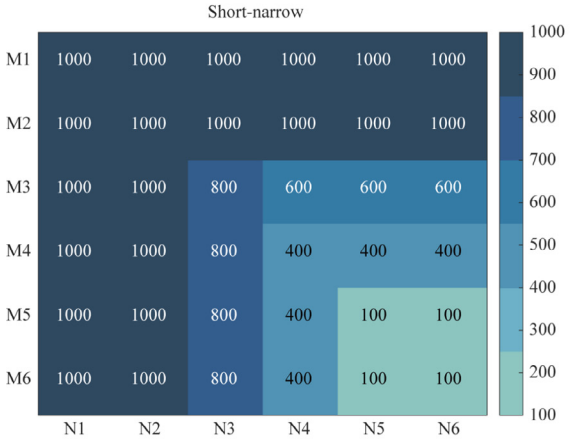

(e) Irradiance distribution of short-narrow shading for 6×6 hybrid PV-TEG systems

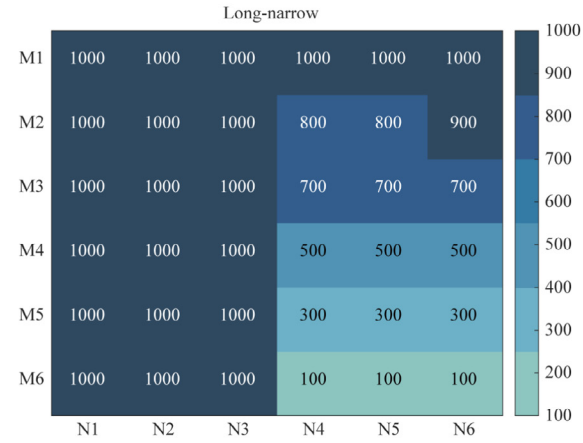

(f) Irradiance distribution of long-narrow shading for 6×6 hybrid PV-TEG systems

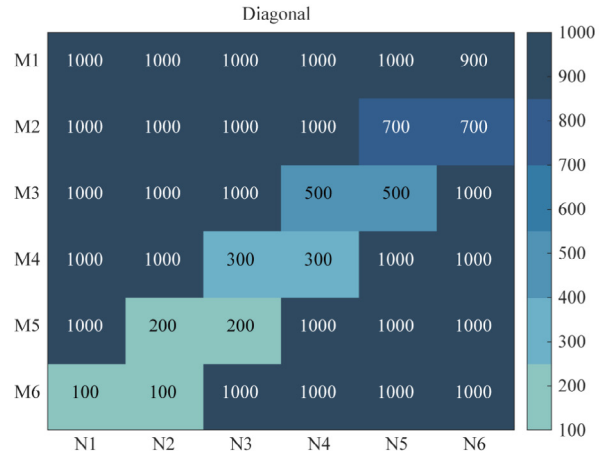

(g) Irradiance distribution of diagonal shading for 6×6 hybrid PV-TEG systems

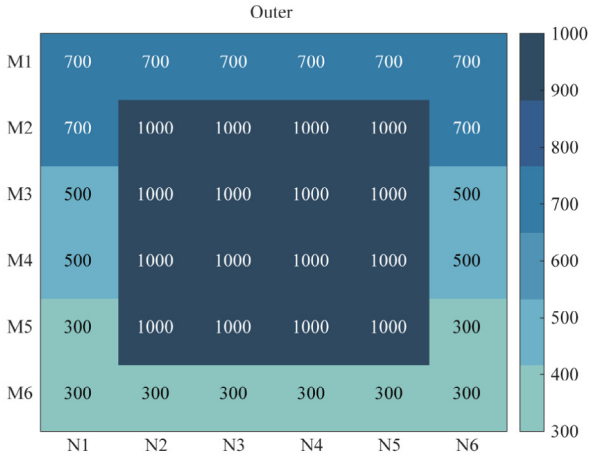

(h) Irradiance distribution of outer shading for 6×6 hybrid PV-TEG systems

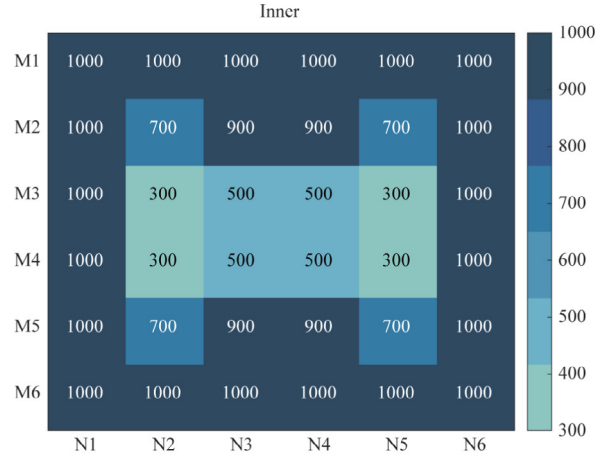

(i) Irradiance distribution of inner shading for 6×6 hybrid PV-TEG systems

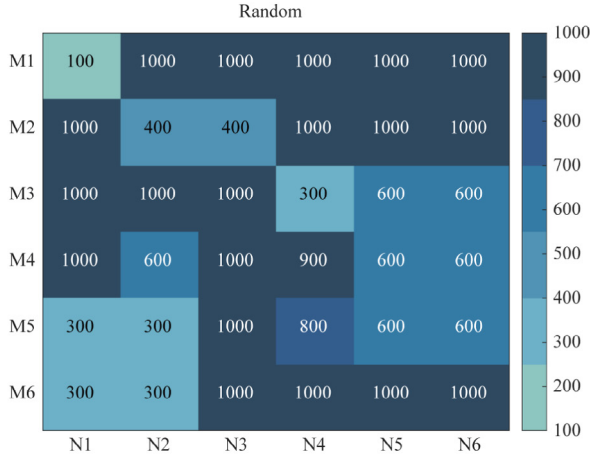

(j) Irradiance distribution of random shading for 6×6 hybrid PV-TEG systems

References

[1] B. Yang, R.Y. Zheng, Y.M. Han, J.X. Huang, M.W. Li, H.C. Shu, S. Su, Z.X. Guo, Recent advances in fault diagnosis techniques for photovoltaic systems: a critical review, Prot. Control Mod. Power Syst. 9 (3) (2024) 36–59.

[2] S.S. Choudhary, T.N. Gupta, Optimal control of single-phase microgrid with photovoltaic and energy storage for improving operation performance and seamless state transition, Energy Convers. Econ. 6 (5) (2025) 324–340.

[3] B. Yang, R. Xie, H.C. Shu, Y.M. Han, C. Zheng, H. Hu, E.B. Luo, Y.X. Ren, L. Jiang, Y.Y. Sang, Techno-economic-environmental optimization of hybrid photovoltaic-thermoelectric generator systems based on data-driven approach, Appl. Therm. Eng. 257 (2024) 124222.

[4] M. Haghighat, M. Niroomand, H.D. Tafti, C.D. Townsend, T. Fernando, A review of state-of-the-art flexible power point tracking algorithms in photovoltaic systems for grid support: classification and application, J. Mod Power Syst. Clean Energy 12 (1) (2024) 1–21.

[5] Y. Wang, Z.G. Li, R.N. Xu, Adaptive battery scheduling strategy for photovoltaic-thermal systems under stochastic irradiance, J. Mod Power Syst. Clean Energy 12 (2) (2024) 234–247.

[6] S.K. Pathak, P.O. Sharma, V. Goel, S. Bhattacharyya, H.S. Aybar, J.P. Meyer, A detailed review on the performance of photovoltaic/thermal system using various cooling methods, Sustain. Energy Technol. Assess. 51 (2022) 101844.

[7] W. Wei, N. Li, L. Che, Y. Fan, H. Liu, J. Ji, B. Yu, A continuous 24-hour power generated PV-TEG-PCM hybrid system enabled by solar diurnal photovoltaic/thermal conversion and nocturnal sky radiative cooling, Energ. Conver. Manage. 321 (2024) 119086.

[8] A.K. Gupta, B.S. Reddy, J.H. Kim, Hybrid energy harvesting systems: Coordinated optimization of PV-thermoelectric generators using adaptive twin-delayed DDPG, Prot. Control Mod. Power Syst. 19 (1) (2024) 112–125.

[9] P. Aravind, D.P. Winston, S. Sugumar, M. Pravin, Optimal battery based electrical reconfiguration technique for partial shaded PV system, Appl. Energy 361 (2024) 122942.

[10] F. Selimefendigil, H.F. Oztop, Optimization assisted divide-combine approach to model cooling of a PV module equipped with TEG by using a trapezoidal shaped hybrid nano-enhanced

cooling channel and performance estimation with generalized neural networks, Int. J. Heat Mass Transf. 241 (2025) 126757.
[11] Z.J. Zhang, B. Yang, H.B. Li, et al., Dynamic voltage compensation for thermoelectric generation systems based on double q-learning, Power Syst. Technol. 49 (8) (2025) 3354–3361, https://doi.org/10.13335/j.1000-3673.pst.2025.0068.
[12] B. Yang, Z.J. Zhang, J. Zhang, X.L. Cheng, J.L. Li, J.L. Shu, J.N. Wang, X.T. Wang, Y.L. Li, J.B. Wang, Optimal reconfiguration design and HIL validation of hybrid PV-TEG Systems via improved firefly algorithm, Energy 286 (2024) 129648.
[13] C. Shao, A. Migan-Dubois, D. Diallo, Performance of BIPV system under partial shading condition, Sol. Energy 283 (2024) 112969.
[14] K. Rasool, J. Mohsin, L.M. Tarig, An improved perturb and observed maximum power point tracking algorithm for photovoltaic power systems, J. Mod Power Syst. Clean Energy 11 (4) (2023) 1165–1175.
[15] P. Murugesan, P.W. David, P. Murugesan, N.K. Solaisamy, One-step adaptive reconfiguration technique for partial shaded photovoltaic array, Sol. Energy 268 (2023) 111949.
[16] B. Yang, Y.L. Li, J.X. Huang, M.W. Li, R.Y. Zheng, J.H. Duan, T.S. Fan, H. Zou, T. Liu, J.B. Wang, H.C. Shu, L. Jiang, Modular reconfiguration of hybrid PV-TEG Systems via artificial rabbit algorithm: modelling, design and HIL validation, Appl. Energy 351 (2023) 121868.
[17] A. Alharbi, A. Fathy, H. Rezk, M.A. Abdellakareem, A. Olabi, An efficient war strategy optimization reconfiguration method for improving the PV array generated power, Energy 283 (2023) 129129.
[18] X. Gao, F. Deng, G.Q. Wu, Q.F. Pan, C.Y. Zheng, W. Wang, T. W. Cai, L.Y. Jiang, Divide and Conquer Q-Learning (DCQL) algorithm based photovoltaic (PV) array reconfiguration scheme for alleviating the partial shading influence, Sol. Energy 249 (2023) 21–39.
[19] A. Alharbi, H. Rezk, M.A. Abdelkareem, A.G. Olabi, Dynamic electrical reconfiguration of PV arrays with integrated battery storage using war strategy optimization, Energ. Conver. Manage. 292 (2023) 117385.
[20] W.Z. Zhang, C.B. Xu, Capacity configuration optimization of photovoltaic-battery-electrolysis hybrid system for hydrogen generation considering dynamic efficiency and cost learning, Energy Convers. Econ. 5 (2) (2024) 73–131.
[21] B. Tian, Z. Guo, B. Zhou, L. Fan, Z. Deng, Y. Zhang, Z. You, L. Lin, A distributed model-free adaptive voltage control algorithm for distribution systems with extensive integration of photovoltaics, Energy Convers. Econ. 6 (1) (2025) 54–63.
[22] X. Gao, D. Ning, J. Chen, T. Meng, B. Xu, H. Zhang, Low-carbon park energy scheduling via PPO-Mix clip reinforcement learning with hybrid PV-battery reconfiguration, Renew. Energy 225 (2024) 120235.
[23] C.X. Jiang, Z. Lin, C.X. Liu, F.X. Chen, Z.G. Shao, MADDPG-based active distribution network dynamic reconfiguration with renewable energy, Prot. Control Mod. Power Syst. 9 (6) (2024) 143–155.
[24] L.S. Guo, Z.Y. Chen, M.H. Yin, C.X. Cai, Y. Zou, Maximum power point tracking control of wind turbine generators based on high-order torque curve, J. Mod Power Syst. Clean Energy 13 (3) (2025) 865–877.
[25] G. Bektur, A reinforcement learning-based multiobjective heuristic algorithm for multiple-truck routing problems with heterogeneous drones, Appl. Soft Comput. 167 (2024) 112290.
[26] R. Mostafa, D. Maeve, A hybrid heuristic-reinforcement learning-based real-time control model for residential behind-the-meter PV-battery systems, Appl. Energy 355 (1) (2024) 122244.
[27] S. Fatih, O. Damla, H.F. Oztop, Energy and exergy performance improvement of coupled PV–TEG module by using different shaped nano-enhanced cooling channels, Renew. Energy 234 (2024) 121059.
[28] S.M. Al Shurafa, F.B. Ismail, H.A. Kazem, T.E. Sann, T.A.H. Almajali, Enhancing photovoltaic-thermoelectric generator (PV-TEG) system performance via mathematical modeling and advanced thermal interface material: an emphasis on pyrolytic graphite sheet (PGS), Sol. Energy 273 (2024) 112514.
[29] E. Yin, Q. Li, Achieving extensive lossless coupling of photovoltaic and thermoelectric devices through parallel connection, Renew. Energy 193 (2022) 565–575.
[30] Y.T. Wang, B. Yang, Optimal PV array reconfiguration under partial shading condition through dynamic leader based collective intelligence, Prot. Control Mod. Power Syst. 8 (3) (2023) 646–661.
[31] W. Hu, S. Wang, P.L. Du, An optimized distribution model for energy system in virtual power plants integrating electric vehicles based on TD3 and DQN, Prot. Control Mod. Power Syst. 10 (6) (2025) 31–48.
[32] T. Tan, H. Xie, Y.N. Xia, X.Y. Shi, M.S. Shang, Adaptive moving average Q-learning, Knowl. Inf. Syst. 66 (2024) 7389–7417.
[33] B. Yang, B.X. Liang, S.C. Wu, H.B. Li, D.K. Gao, L. Jiang, J.B. Wang, Optimal power extraction of PV-TEG hybrid system via fitness-distance-balance-based beluga whale optimization, Global Energy Interconnect. 8 (1) (2025) 43–61.
[34] I.U. Khalil, M. Jalal, A. Ul Haq, M. Ahasan, U. Ghumman, Fuzzy logic-controlled battery-assisted reconfiguration for partial shaded PV systems, J. Storage Mater. 86 (2024) 111452.
[35] J.B. Wang, Y.L. Li, B. Yang, L. Jiang, Multi-optimized reconfiguration of hybrid photovoltaic-thermoelectric generation (PV-TEG) system for performance enhancement, Energ. Conver. Manage. 307 (2024) 118373.
[36] Y.H. Yang, W. Pei, T.Y. Xu, D.W. Wang, A. Redouane, Federated dueling deep Q-network based collaborative energy scheduling for a power distribution network, Energy Convers. Econ. 6 (3) (2025) 141–212.
[37] B. Yang, J.R. Wang, S. Su, Y.L. Li, P.Y. Wu, Z.W. Yang, H. Fan, W.T. Li, J.L. Li, Mismatch losses mitigation of hybrid PV-TEG Systems via improved RIME algorithm: design and hardware validation, J. Clean. Prod. 434 (2024) 139957.
[38] H. Qin, T. Meng, K. Chen, Z. Li, A comparative study of DQN and D3QN for HVAC system optimization control, Energy 307 (2024) 132740.
[39] Y.L. Wu, L. Ge, X.D. Yuan, X.Y. Fu, M.S. Wang, Adaptive power control based on double-layer Q-learning algorithm for multi-parallel power conversion systems in energy storage station, J. Mod Power Syst. Clean Energy 10 (6) (2022) 1714–1724.
[40] H.Q. Chen, Y.D. Liu, Z.T. Zhou, M. Zhang, A2C: attention-augmented contrastive learning for state representation extraction, Appl. Sci. 10 (17) (2020) 5902.

Lei Zhou received Bachelor's degree in Electrical Engineering from Kunming University of Science and Technology. He enrolled in graduate studies at Kunming University of Science and Technology in 2024. His research interests include dynamic reconfiguration of renewable energy systems.